chemistry

MDPI

Review

A Comprehensive Review on Hydrothermally Tuning $SrTiO_3$ for Efficient Photocatalytic Applications: Water Remediation and Water Splitting

Soujanya Nethi [1], Pallavi Saxena [2] and Anupam Singha Roy [2,*]

[1] School of Technology, Woxsen University, Hyderabad 502345, India; soujanya.n@woxsen.edu.in
[2] School of Sciences, Woxsen University, Hyderabad 502345, India; pallavi.saxena@woxsen.edu.in
* Correspondence: anupam.singharoy@woxsen.edu.in

Abstract

Global requirement of clean, cost-effective and sustainable energy has stimulated massive research and development in photocatalytic materials that have the potential to harvest solar based energy while mitigating the environmental issues. Among various materials, perovskite oxides have emerged as a promising energy resource. Owing to the structural versatility, optical and electrical properties, chemical inertness allows the use of material of multifunctional prospects. Currently Strontium titanate ($SrTiO_3$), a vital perovskite oxide having a band gap nearly ~3.2 eV, is showing significant function for photocatalytic water splitting, carbon dioxide conversion and degradation of organic pollutants. Though within the UV spectrum, its intrinsic photocatalytic behavior is limited to approaches such as graphene junctions, noble-metal support, and post-synthetic heat treatment seem to promote the adsorption within visible-light. Strontium titanate also demonstrates photo charge separation efficiency, and long-term catalytic durability. Moreover, modifications and hydrothermal synthesis have proven extremely efficient for nano-based engineering, control over crystal diameter, defects, and shape, which can result in magnificent composites that can be promising substitutes. Therefore, further research is imperative regarding these material application prospects. This comprehensive review provides insights into details on the potential of nanoengineering and composite approaches to reduce the inherent limitations of perovskite oxides, especially Strontium titanate, and enabling additional applications in next-generation photovoltaic and solar energy harvesting technologies.

Keywords: perovskite oxides; photocatalysis; water splitting; nanoengineering; environmental remediation; charge separation efficiency

Check for updates

Academic Editor: Detlef W. Bahnemann

Received: 20 May 2026
Revised: 29 June 2026
Accepted: 2 July 2026
Published: 6 July 2026

Copyright: © 2026 by the authors. Licensee MDPI, Basel, Switzerland. This article is an open access article distributed under the terms and conditions of the Creative Commons Attribution (CC BY) license.

1. Introduction

One of the major prominent challenges faced by the world in the early 21st century is to satisfy the global energy demand while simultaneously reducing the emission of harmful gasses into the atmosphere, as well as various pollutants into barren lands and into water bodies. As per the International Energy Statistics (IES), almost 80% of the world's energy needs are being satisfied by non-renewable energy, i.e., nearly equal to 293 TwH, and this is going to increase up to 40% by the year 2040 [1]. Continuous use of fossil fuels as the primary source of energy may increase the risk of pollution and also have harsh effects on our planet, potentially increasing the problem of global warming. To answer these challenges, different techniques that can produce and store energy by reducing the

emission of carbon into the atmosphere have been developed. At present, the world is turning to renewable energy sources like solar, wind, geothermal, biomass, etc. to fulfill its energy demand. As per the renewables global status report of September 2022, almost 28% of the world's energy demand is satisfied by renewable energy [2]. Although a significant amount of research has already been started in this area, there are some questions that remain unanswered by the research community, such as:

- What could increase energy conversion efficiency?
- Are the required materials available abundantly and cost effective?
- What could be the installation cost of the production grid, as it is all-new technology?
- Are laboratory technologies feasible for industrial production?

With abilities like cost effectiveness, better efficiency, and non-emissive fuel conversion, environmental catalysis is a technique that can answer the above questions. It mainly requires catalysts that are readily available, and that are thermally and chemically stable. Perovskite oxides are a class of materials arranged in a perovskite structure, allowing different composition of elements. These materials can be easily synthesized, and their structure and properties can be modified so that they can be used in different applications [3–7]. With this unique ability these perovskite oxide materials can be implemented as catalysts in an environmental catalysis. While designing a perovskite oxide with better efficiency and performance, many factors are considered that come into existence for a particular selected application. According to the literature, properties of perovskite oxide can be varied by substituting the lattice atoms via doping with a foreign material to enhance the opto-electrical properties [8–11]. Hence the chemical composition of perovskite oxide plays a crucial role in making it applicable for catalysis.

Performance of catalysts is also affected by their structure and morphology. As we already know, nanostructures always have better activity compared to the bulk ones. Also, different morphologies in the nanoscale range and the porous structures of the perovskite oxides, having properties like large surface area, ease of separating charge carriers, a greater number of active sites, lower recombination rates, less diffusion lengths, etc., can lead to exhibiting an efficient performance as a catalyst material [12–16]. Along with the above factors, the post processing of the perovskite oxides, in addition to their bottom-up synthesis, can change the properties like band gap, structure, carrier mobility etc. [17].

Among the different perovskite oxides, $SrTiO_3$ is one which has a band gap of 3.2 eV (Figure 1a). It has a mixed ionic and electronic conductivity (MIEC) and showed good stability under high temperature and chemical inertness, which makes it suitable for a wide range of applications [18–21]. Even though due to the wide band gap of $SrTiO_3$, it cannot be utilized into catalysis directly, but its properties can be tailored by either doping, post heat treatment, or decorating with noble metals or graphene, etc., to make it suitable for the application.

Photocatalytic materials composed of nanostructured perovskite oxides, with $SrTiO_3$ being the most common, have been successfully synthesized in several morphological configurations including powder-based particles and films. The powder form of $SrTiO_3$ is represented by nanoparticles, nanorods, nanocubes, and hierarchical structures; however, the most important advantage of this morphology lies in the specific surface area, easy adjustment of the surface structure and possibility of introduction of dopants and co-catalysts. Thus, the powder-based $SrTiO_3$ is a widespread choice for photocatalytic degradation of pollutants in solution and for photocatalytic hydrogen production. At the same time, thin films of $SrTiO_3$, produced via pulsed laser deposition, magnetron sputtering, atomic layer deposition and sol–gel spin-coating techniques, have a completely different set of features that makes them attractive: immobilization on a substrate solves the problem of catalyst recycling after reaction, restriction of the thickness of the film at the atomic scale

prevents the carrier recombination inside the film and the strain effect allows tuning the band alignment to increase the driving force of surface reactions. These attributes make $SrTiO_3$ thin films a particularly promising strategy for environmental remediation and solar energy conversion applications [21].

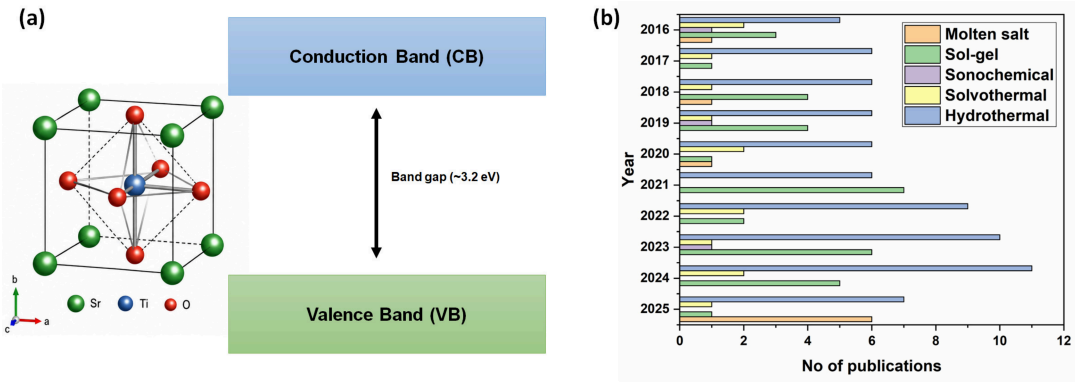


Figure 1. (**a**) Perovskite crystal structure of $SrTiO_3$ and electronic band diagram illustrating conduction and valence band positions, (**b**) Tendency of research publications on $SrTiO_3$ and their different synthesis procedures.

$SrTiO_3$ has recently gained prominence as a major category of photocatalysts due to their chemical stability, versatile electronic properties, and the possibility of band-gap tuning via doping and heterostructure formation. Several methods for the synthesis of $SrTiO_3$ systems have been developed, including solid-state synthesis, sol–gel technique, co-precipitation, molten-salt synthesis, sonochemistry, and hydrothermal and solvothermal syntheses [22–28]. In particular, $SrTiO_3$ obtained using the solid-state and molten-salt methods possesses a rather large particle size and low specific surface area and is synthesized at temperatures above 1000 °C, resulting in low density of active sites on its surface. Sol–gel and co-precipitation syntheses give fine particles but often lead to formation of amorphous or polycrystalline powders that have to be subsequently annealed in order to achieve the desired crystallographic phase, which leads to uncontrollable grain growth. Hydrothermal synthesis stands out from other methods because it allows one to obtain pure-phase particles of high surface area at temperatures ranging from 120 to 220 °C, along with fine-tuning of the morphology, dopant incorporation, and hydroxyl content. These attributes make hydrothermal synthesis uniquely suited to produce the well-defined, compositionally controlled materials needed for systematic photocatalytic studies. The increasing research importance in $SrTiO_3$ and their different synthesis procedures were retrieved from PubMed in a time frame of 2016 to 2025 (Figure 1b). The growth in publications implies the progress of $SrTiO_3$ and their emerging applications.

This work focuses on the post heat treatment of hydrothermally synthesized $SrTiO_3$ and the synthesis of forming nanocomposites to tailor its properties for use as a catalyst. A one step hydrothermal synthesis route was discussed for the synthesis of $SrTiO_3$ nano cubes with variation in synthesis temperature. Additionally, a post calcination step was also elaborate to study its impact on the synthesized material. Obviously, the rise in temperature increased the crystallite size and calcination treatment decreased the band width of the material, so that the absorption peak shifted from the UV region to the visible region, corresponding to a band energy of 3.2 eV. This review also explains the effect of forming nanocomposites of $SrTiO_3$ with Ag nanoparticles and graphene oxide, where Ag nanoparticles were synthesized using the citrate reduction technique and mounted onto the freshly formed $SrTiO_3$ cubes to determine their photocatalytic properties. Similarly, a

nanocomposite of $SrTiO_3$ and graphene oxide was synthesized via modified Hummer's method and tested for photocatalytic properties.

This review presents the study of hydrothermally synthesized $SrTiO_3$ as a photocatalyst for environmental purification and water splitting using solar energy. The selection of $SrTiO_3$ as a semiconductor is based on its stable structure, adjustable band gap, and flexible compositions. In order to enhance the activity of $SrTiO_3$ under visible light, which cannot be achieved due to its only photoactivity under UV irradiation, three ways are adopted, including: hydrothermal synthesis at different temperatures, post-synthesis annealing for narrow band gap, and the formation of nanocomposites. These approaches establish a clear relationship between structure–property and performance, laying a foundation for rational design of next-generation perovskite photocatalysts targeting sustainable hydrogen production and wastewater remediation.

2. Background

2.1. Perovskite

In 1839, the perovskite mineral $CaTiO_3$ was discovered in the Ural Mountains by Russian minerologist Gustav Rose and named after Count Lev Aleksevich von Perovski [29]. The structure of perovskite ABX_3 was only described in 1926 by Victor Goldschmidt, where A and B are cations and X is anion [30]. A is a cation with a 12-fold cuboctahedral site and B is a smaller cation, which is occupies a 6-fold coordinated octahedral site. This is typically implemented in perovskite oxides. A-site is occupied by Alkaline earth metal ions like Sr^{2+}, Ca^{2+}, Ba^{2+}, etc., and rare earth metal ions like La^{3+}, Nd^{3+}, etc. Transition-metal cations like Ti^{2+}, Fe^{3+}, Mn^{3+}/Mn^{3+}, Co^{3+}, or Ni^{3+} are in the B-site. The X-site in the perovskite structure is occupied by oxygen (O^{2-}) ions, that form a network of corner-sharing BX_6 octahedra. These oxygen anions, through their interaction with the B-site cations, play a major role in maintaining structural stability. They also influence the electronic, optical, and catalytic properties of the material. The stability of the perovskite structure is determined by Goldschmidt tolerance factor by assessing the ionic radii and oxidation states of the constituent ions [30].

A perovskite material can have different crystal structures like cubic, tetragonal, and cuboctahedral, rombohedral (Figure 2). It can also have a transition from one crystal structure to another without any deformation and with a tolerance factor known as the Goldschmidt tolerance factor given by parameter t, as shown in Equation (1):

$$t = \frac{r_A + r_X}{\sqrt{2}(r_B + r_X)} \quad (1)$$

where r_X is the radius of anion and r_A and r_B are the radii of A and B cations, respectively [31]. Based on the findings, cubic perovskites are typically assigned t values close to unity ($0.9 < t < 1.0$), while orthorhombic or rhombohedral symmetries are observed within the range of $0.8 < t < 0.9$ and fully distorted Orthorhombic perovskite possess value ranges between $0.71 < t < 0.80$ [30].

When the relative size of the A-site cation is not sufficiently large compared to the B-site cation, lower t values are observed. In such cases, the BX_6 octahedra tilt in order to occupy the empty space between them, resulting in a loss of symmetry. The tilting of the octahedra about the b and c axes leads to an orthorhombic structure, whereas tilting about each axis results in a rhombohedral structure. The perovskite phase offers flexibility, allowing for only slight deviations from ideal cubic symmetry. In fact, in many cases, a minor tilting of the anionic octahedra can be beneficial for tailoring the electronic and dipole properties of the material, as well as influencing the strength and length of the B-X bonds.

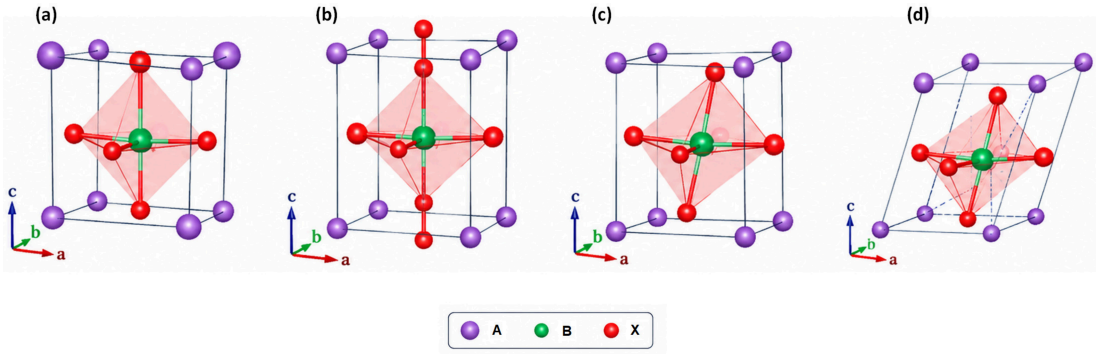


Figure 2. Crystal structures of ABX_3 perovskites with different symmetries: (**a**) cubic perovskite structure with the ideal arrangement of A-site cations at the cube corners, B-site cations at the body center, and X-site anions at the face centers; (**b**) tetragonal perovskite structure characterized by elongation or compression along one crystallographic axis resulting from octahedral distortions; (**c**) orthorhombic perovskite structure exhibiting distortion and tilting of BX_6 octahedra due to ionic size mismatch and lattice distortions; and (**d**) rhombohedral perovskite structure formed by cooperative rotation and tilting of BX_6 octahedra, leading to a reduction in crystal symmetry [13].

The perovskite structure allows for partial replacement of cations at the A- and B-sites with foreign cations, while maintaining the long-range order. This type of substitution is commonly referred to as dopant incorporation with the concentration of foreign cations of 1–10%. When foreign cations have the same valence as the native species they replace in the perovskite lattice, this is referred to as isovalent substitution. In isovalent substitution, the changes in material properties mainly result from size effects, as the different ionic radii of the substituted cations may cause distortions or tilting of the octahedral framework. On the other hand, acceptor or donor substitution refers to the replacement of native sites with foreign cations that have either lower or higher valence, respectively. Acceptor substitution introduces cations with a lower valence compared to the original species, resulting in an increase in electron density and the formation of electron "holes" in the material. Donor substitution involves the incorporation of cations with a higher valency, leading to an excess of electrons. These types of substitution can significantly alter the material properties by simultaneously introducing size effects and modifying the electronic characteristics of the perovskite structure.

The empirical Hume–Rothery solubility rules, originally formulated for metal alloys, can also be applied to the substitution of ions in inorganic and mineral systems [31]. In the hypothetical $M_xA_{1-x}BX_{3\pm\delta}$ perovskite system, the probability of forming a substitutional solid solution is highest under the following conditions:

- The MBX_3 and ABX_3 parent phases crystallize in the same or identical structure. This similarity in crystal structure allows for the efficient substitution of M cations into the A-sites, maintaining the overall structural integrity of the perovskite lattice.
- The ionic radii and electronegativity values of the cations M and A are similar. When the sizes and electronegativities of the substituting cations (M) and native cations (A) are comparable, it promotes their compatibility within the perovskite lattice. Similar ionic radii help to minimize lattice strain and distortion, while comparable electronegativities facilitate the maintenance of charge balance in the structure.
- The substituting M cations and native A cations have the same valence. When the valence states of the substituting and native cations match, it ensures that the charge balance is preserved in the perovskite structure. This is important for maintaining the overall neutrality and stability of the material.

By satisfying these criteria, the probability of forming a substitute solid solution in the $M_xA_{1-x}BX_{3\pm\delta}$ perovskite system is maximized, enabling the incorporation of M cations

into the A-sites while preserving the structural and chemical integrity of the material. When the aforementioned conditions are fully satisfied, it is likely that a continuous solid solution spanning the entire range between ABX_3 and MBX_3 will be formed. In this case, the native and substituent (solute) cations are randomly distributed within the designated sites, resulting in a single perovskite phase. However, if the conditions are only partially fulfilled, a solid solution may be observed up to a certain level of substitution. Beyond this point, a phase transition or segregation may occur. This is particularly common in the case of aliovalent substitution, where the replacement of cations introduces an extra charge that needs to be counterbalanced. In ionic solids, this additional charge is typically compensated by the formation of defects in the crystal lattice, such as vacant sites that are normally occupied. The diffusion of charged or neutral species within crystalline solids is directly influenced by the type and number of defects present in the lattice [32]. Therefore, the rational substitution of A- and B-site cations can lead to significant modifications in the defect structure, which can have substantial implications for the functional properties of the material. The perovskite structure's flexibility provides extensive opportunities for material engineering in the field of environmental catalysis. By carefully controlling the substitution of A- and B-site cations, it becomes possible to tailor the material's properties and optimize its performance in various catalytic applications.

2.2. Strontium Titanate ($SrTiO_3$ or ST)

Tausonite, a naturally occurring mineral, was first discovered in Siberia in 1982. It belongs to the well-known class of perovskite compounds and has the chemical formula $SrTiO_3$. Tausonite is named after the Russian geochemist Lev Vladimirovich Tauson. In its synthetic form, $SrTiO_3$ is recognized as an ideal cubic perovskite, characterized by a lattice parameter of a = 3.905 Å at room temperature. The synthetic material has a mass density of $\rho = 5.12$ g cm^{-3}. The discovery of a naturally occurring $SrTiO_3$ mineral, or tausonite, expanded our understanding of perovskite compounds and their occurrences in nature [33]. Within the cubic lattice of $SrTiO_3$, small deviations from the nominal stoichiometry can be accommodated. Specifically, slight excesses of Strontium within the structure can be incorporated as local Ruddlesden–Popper phases, characterized by a general composition of $Sr_{n+1}Ti_nO_{3n+1}$ [34]. These local phases exhibit a tetragonal symmetry group known as I4/mmm, as shown in Figure 3. Additionally, excess oxygen can also form extended defects within the lattice, resulting in oxygen-rich regions. These small variations from the ideal stoichiometry demonstrate the flexibility of the $SrTiO_3$ lattice in accommodating structural deviations while maintaining its overall perovskite framework.

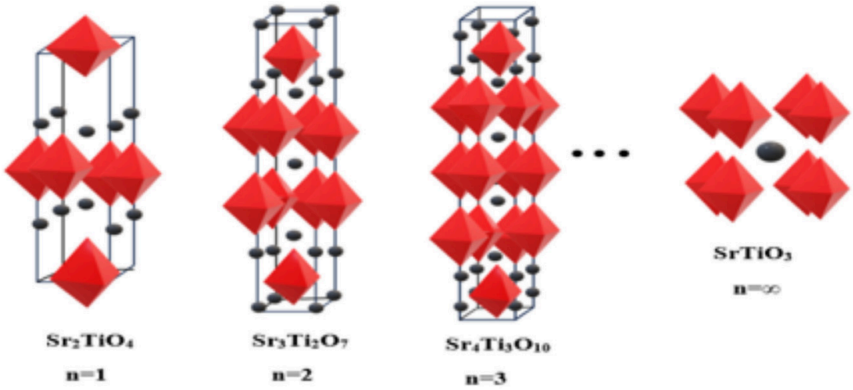


Figure 3. Unit cells of $Sr_{n+1}Ti_nO_{3n+1}$ [34].

$SrTiO_3$ is a material that exhibits various phases and symmetries depending on temperature and doping. At high temperatures, up to its melting point of 2080 °C, $SrTiO_3$

maintains its cubic symmetry [35]. However, upon cooling or doping with foreign ions, transitions to lower symmetries can occur. Between the temperature range of 110 K and 65 K, $SrTiO_3$ crystals undergo a phase transition from cubic to tetragonal symmetry [36]. This transition results in material acquiring a dipole moment and approaching ferroelectricity. The dipole moment arises from the breaking of the cubic symmetry, leading to the development of electric polarization within the material. Further cooling below 65 K, between 55 K and 35 K, results in an orthorhombic symmetry in $SrTiO_3$ [37]. At even lower temperatures below 10 K, there is a possibility of the material exhibiting rhombohedral symmetry [38]. These changes in symmetry indicate the presence of different crystal structures as the temperature decreases. In the cubic phase, $SrTiO_3$ is a charge symmetric and paraelectric material, indicating that it does not possess a permanent electric dipole moment. However, with the transition to the tetragonal phase, it gains a dipole moment and becomes closer to being ferroelectric. The dielectric permittivity (ε) of $SrTiO_3$ is already high, and it increases linearly with decreasing temperature, following the Curie–Weiss law. Between room temperature and approximately 1.4 K, the dielectric permittivity of $SrTiO_3$ increases from 370 to around 1.4×10^4 [39]. This behavior indicates the enhanced response of the material to an applied electric field at lower temperatures. Doping $SrTiO_3$ with certain elements can induce superconductivity at extremely low temperatures at around 1 K. The doped $SrTiO_3$ exhibits superconducting properties, which means it can conduct electricity without resistance at those temperatures. $SrTiO_3$ substrates are known for their excellent compatibility with the epitaxial growth of high-temperature superconductors. Epitaxial growth refers to the process of depositing a crystal layer on a substrate with matching lattice parameters and orientation, allowing for the formation of high-quality crystal structures. The use of $SrTiO_3$ substrates facilitates the growth of high-temperature superconducting materials which exhibit superconductivity at temperatures higher than conventional superconductors. It is also significant to highlight that $SrTiO_3$ perovskites belong to the class of mixed ionic-electronic conductors (MIECs). According to Saraf et al., these materials showed remarkable stability in varied conditions [40]. As a result, $SrTiO_3$ has gained importance as a model material and has been the focus of in-depth research into the chemistry of its defects for the past few decades [41–43]. $SrTiO_3$-based perovskites have been shown to be quite useful in a variety of applications that generate a lot of research interest. Solar cells, hydrogen production, oxygen sensors, fuel cell electrodes, oxide electronics, and oxygen separation membranes are a few of these uses.

3. Synthesis Methods for Perovskite Oxides

The catalytic performance of perovskite oxides is dependent on a wide range of material properties, including mixed oxidation states demonstrated by their B-site cations, the mobility of oxygen within the structure, and the quantity and reactivity of available active sites [12,44,45]. The nanostructure and morphology of the material, together with its chemical composition, are equally important elements in determining these parameters and consequently impacting the catalytic efficacy of the material. Nanostructured perovskite oxide catalysts with mesoporous morphologies outperform bulk counterparts in a variety of ways. These benefits originate from their large surface areas and reduced diffusion length of carriers, leading to a higher density of reactive sites, enhanced redox characteristics, greater oxygen mobility, and reduced carrier recombination [46]. As a result, a diverse design strategy is required to create high-performance perovskite oxide catalysts that include porosity, controlled cationic substitution, nanostructure, and defect structure engineering.

Perovskite oxides are normally produced using a solid-state method, where precursor salts or individual metal oxides are physically blended and then exposed to high-temperature sintering (usually above 1000 °C). This approach requires prolonged heating

times ranging from 8 to 24 h to obtain the requisite phase purity [47]. Furthermore, the final product frequently has flaws such as insufficient homogeneity, a wide range of particle sizes, and unsatisfactory textural qualities [48]. Despite these challenges, the solid-state synthesis technique is nevertheless commonly used for the manufacture of perovskite oxides due to its simplicity. Several alternative synthesis approaches have been developed to overcome these concerns by reducing the extremely high reaction temperatures and promote nanostructure formation. While common synthesis methods at intermediate temperature, such as co-precipitation and evaporation-induced self-assembly (EISA), are generally compatible with single metal oxides, they often face difficulties when employed with mixed metal oxides due to variances in metal solubility and reactivity. There have been examples in the literature where researchers have successfully described perovskite oxide synthesis applying the above procedures [49–51].

Because of its numerous advantages, such as simplicity, high purity, and rapid reaction rates, auto combustion synthesis is a popular approach. In this procedure, cationic precursors are combined with a solvent and a fuel/oxidizer. Following solvent evaporation, the gel is heated on a heating plate or in a muffle furnace until the highly exothermic auto combustion reaction begins, resulting in the desired perovskite material. Urea, glycine, glycerol, and alanine are common fuels employed in this process. The surface area of the resultant materials typically ranges from 5 to 40 m^2/g. Despite its simplicity and scalability, auto combustion synthesis has certain drawbacks. It usually requires quite high reaction temperatures, around 800 °C, and provides limited control over the calcination conditions. As a result, attaining accurate nanostructures with this approach might be difficult. When using this process to synthesize multicomponent oxides, the resultant materials may contain impurities. In the synthesis of $SrTi_{0.5}Fe_{0.5}O_3$, there were impurity phases, notably $Sr_3Fe_2O_7{}^-$ and TiO_2, irrespective of the precise reaction parameters using glycine and metal nitrates as precursors [52]. Methods like pulsed laser deposition, chemical vapor deposition and molecular beam epitaxy can also be employed, but these techniques utilize complex and expensive equipment.

3.1. Hydrothermal Synthesis of Perovskite Oxides

Hydrothermal or solvothermal is a suitable method for synthesis, and a small variation in either temperature, time, concentration of solvents, etc., can help in modifying the morphology of the synthesized materials. Solvothermal chemistry has become a well-known tool for synthesizing nanomaterials. The hydrothermal conditions were initially investigated for reasons such as the synthesis of silicate zeolites, replicating geological conditions for mineral formation in the Earth's crust, and controlling the growth of dense minerals such as quartz. Water has peculiar qualities when heated in a sealed vessel to generate pressure. In synthetic chemistry, factors such as ionic strength, viscosity, dielectric constant, and density play critical roles in regulating reagent solubility, nucleation rate, and crystal growth. Even at temperatures considerably less than the critical point of water (374 °C and 218 atm), alterations to a reaction medium take place in relation to the surrounding environment, promoting the chemical decomposition and reaction required for complicated material crystallization. Many hydrothermal synthesis processes mentioned in the literature use temperatures that are below 250 °C. Rabenau's initial paper thoroughly covered hydrothermal chemistry's key role in synthesis and its adaptability across numerous classes of materials, ranging from oxides, halides, nitrides, chalcogenides, and metals [53]. Numerous research groups have stressed the importance of hydrothermal methods in the synthesis of oxide materials [54–59]. In contrast, other studies have emphasized the use of non-aqueous solvents as an alternative technique in this situation. Several important advantages emerge by opting hydrothermal techniques such as:

Particle Characteristic Precision: Hydrothermal synthesis allows for the creation of finely adjusted powders with control over a broad spectrum of morphologies from nano- to micro-scale. This approach has a particular benefit in terms of exact regulation of particle size and form.

Metastability Unveiling: Hydrothermal procedures have a unique ability to disclose and isolate metastable compounds and structural configurations that are difficult to achieve using typical high-temperature synthesis methods. This capacity allows for the investigation of innovative materials and properties.

Expansion of Structural Diversity: The hydrothermal method opens the way for solid solutions and substitute versions of well-known structural types that would be difficult to obtain using traditional methods. This increased structural diversity improves our ability to customize materials for specific applications and functions.

These benefits highlight the importance of hydrothermal synthesis in furthering our understanding of oxide materials and broadening the possibilities for their customized design and application. The hydrothermal synthesis of $BaTiO_3$ was first described in the 1940s, and Flaschen presented a comprehensive overview of this technique in 1955 [60]. With their initial efforts, there has been an abundance of study into the hydrothermal and solvothermal synthesis of $BaTiO_3$. Fine powders of $Na_{0.5}Bi_{0.5}TiO_3$ and $K_{0.5}Bi_{0.5}TiO_3$ generated through hydrothermal techniques have specific advantages over those prepared via conventional solid-state synthesis, especially when aiming for densified ceramics. However, as previously stated, the presence of flaws can potentially impair the bulk electrical characteristics during subsequent annealing to create ceramics. The photocatalytic features of these hydrothermally produced $Na_{0.5}Bi_{0.5}TiO_3$ nanocubes were investigated [61]. Notably, they displayed the ability to effectively decompose nitric oxide, outperforming a reference TiO_2 catalyst. A direct hydrothermal reaction was used to introduce a low amount of Zr into $Na_{0.5}Bi_{0.5}TiO_3$ [62]. Composites made from finely ground particles of $Na_{0.5}Bi_{0.5}Ti_{0.99}Zr_{0.01}O_3$ demonstrated different properties such as reduced residual polarization and improved piezoelectric responsiveness.

Hydrothermal synthesis appears to be useful in gaining access to more complicated perovskite-related compounds. This approach has been used to successfully synthesize complicated compounds such as $K_2La_2Ti_3O_{10}$ which belongs to the Ruddlesden–Popper family of layered perovskites. These materials can be thought of as intergrowths of perovskite and rock salt. The hydrothermal process formed micro-sized crystallites of $K_2La_2Ti_3O_{10}$ [63], and these crystalline materials have significantly higher photocatalytic activity than their solid-state equivalents. This breakthrough highlights the importance of hydrothermal synthesis in accessing and modifying complex perovskite-related compounds for improved functional applications.

For a variety of A cations, including Ca, Sr, Ba, Pb, and Zn, zirconate and hafnate perovskites, labeled as $AZrO_3$ and $AHfO_3$, have been effectively synthesized by solvothermal methods [64–68]. The process of microwave synthesis has been found to be especially effective in the case of $BaZrO_3$. Longo and colleagues synthesized $BaZrO_3$ as micro-sized Deca-octahedron-shaped crystallites in 40 min at a temperature of 140 °C. Their research presented a crystallization method based on the micro scale self-assemble nanoparticles, with the results depending on the surfactant used as a solution additive. Computational investigation revealed that these materials exhibited unusual photoluminescence features which were attributable to flaws. Borja–Urby's further contributions to hydrothermal synthesis include the creation of Bi/Si-doped samples for use in photocatalytic processes [69]. It is worth noting that the microwave approach has proven to be especially promising for the production of small particles with narrow particle size distributions. Traditional heating methods, on the other hand, have advantages in terms of quicker responses and

need lower temperatures for $BaZrO_3$ crystallization. When a sufficient amount of NaOH is used, Boschini and colleagues showed that solid precipitation occurs at temperatures below 100 °C in just 15 min [70]. Similarly, Yamaguchi et al. demonstrated the crystallization of $BaZrO_3$ and $BaHfO_3$ at 50 °C over a 10-day period using zirconia or hafnia gel and barium hydroxide [71]. However, higher temperatures have been used in the synthesis process as well. Dong et al., for example, heated aqueous KOH solutions of salt precursors at 200 °C for 24 h, resulting in the development of hollow spherical $BaZrO_3$ particles [72].

Kanie and his group reported a novel seeding method that involved heating zirconium oxy-acetate and barium hydroxide in methanol at 200 °C for 24 h [73]. This method produced seed crystals, which were then treated to hydrothermal conditions at 250 °C with a combination of barium hydroxide and a Zr-triethanolamine complex and generated monodisperse spherical crystallites of $BaZrO_3$ [74]. This group investigated the control of particle shape by varying metal ion concentrations, which led to the formation of spherical, rhombic dodecahedral, and flower-shaped $BaZrO_3$ particles. This adaptability allowed for the creation of Eu^{3+}-doped materials with altered photoluminescence characteristics. Zhang and coworkers synthesized Ce^{4+}-substituted $BaZr_{1-x}Ce_xO_3$ materials using aqueous NaOH [75]. These materials were used as sono-catalysts to decompose a simulated organic contaminant. Additionally, the photoluminescence characteristics of Yb^{3+}-doped materials were investigated. Finally, using EDTA as a solvent resulted in the formation of hollow $BaZrO_3$ nanocrystals with higher concentration of oxygen vacancies, which gave photocatalytic capabilities for hydrogen evolution from water [76].

There has been a major increase in demand for the use of solvothermal methods for the synthesis of perovskite oxides during the past decade. This renewed interest draws on previous research on fundamental materials such as $BaTiO_3$, $NaNbO_3$, and rare-earth manganates. Researchers have broadened their investigation to include nearly all compositional variations within the realm of B-site perovskites [77]. This extension has included the construction of heterostructures with interfaces between perovskite and various other structural types, as well as the development of solid solutions that incorporate as many as five different cations [78–81]. A significant portion of this study has been devoted to achieving exact control over the resulting product. Both the size and shape of the crystals have been modified not only through the use of chemical reagents but also through careful control of reaction temperature and duration. In certain cases, sophisticated crystal morphologies have been developed without the use of templating agents [82]. In some circumstances, solution additives have been deliberately added to impact crystallization paths, or non-aqueous solvents have been used to maintain control over the resulting crystal form [83]. The enormous amount of work in this domain, and the significant success in building complex crystal structures, makes it a challenging endeavor to predict how different reaction conditions will influence crystal morphology. Because of variances in cation solubilities and, in certain cases, the presence of redox reactions during the process of crystallization, the ideal set of reagents as well as conditions for one perovskite family may not be readily transferred to another.

The hydrothermal technique for synthesis has become popular in the industrial sector, where massive batch reactors are used to commercially synthesize numerous minerals. Production of zeolites and quartz crystals are two notable examples [84–86]. More recently, a concerted effort has been made to build continuous-flow reactors for the efficient mass synthesis of polycrystalline materials under hydrothermal environment. This study has focused on the development of nanoparticles composed of mixed-metal oxides. These efforts cover a wide spectrum of materials, including perovskites like $BaZrO_3$, $BaTiO_3$, and $Ba_{1x}Sr_xTiO_3$, the latter of which was successfully manufactured at 80 gm/h in a pilot scale. These initiatives highlight the potential of scaling up laboratory-based chemistry to produce

useful materials for industrial and technological applications. As these materials are applied in real world scenarios, the defects in structure and their effect on bulk characteristics become more important. As in the literature, even trace concentrations of hydroxide ions in the perovskite structure, together with charge-balancing vacancies, can have a negative impact on certain electrical characteristics [87]. As a result, future research should examine methods for minimizing or controlling defects, which will facilitate the development of synthetic chemistry optimized for defect management. This will be critical in connecting materials synthesis with the need to develop energy-efficient, environmentally friendly manufacturing processes. Results showed that there is a relationship between the tolerance factor of perovskite materials and their ease of production under moderate hydrothermal conditions [88]. In multi-element systems, hydrothermal synthesis was found to be viable for perovskites with a Goldschmidt tolerance factor near to 1 and negligible fluctuation in A-site radii. Under this moderate reaction environment, we were able to create perovskite materials with a small structural deformation. It is worth emphasizing that these findings are based on solid-state synthesis of the constituent binary oxides, suggesting a possible relationship between crystal structure energetics and synthetic accessibility. Yamaguchi et al. proposed a similar relationship for $BaZrO_3$ and $BaHfO_3$ when using a gel conversion technique at low temperature.

Figure 4 showed the variation in A cation radius with the tolerance factor for $AMnO_3$ and $ACrO_3$ perovskites, indicating both successful and unsuccessful hydrothermal synthesis events. For manganite's, the threshold temperature is set at T < 300 °C, while for chromite's, it is T < 450 °C [89]. This figure illustrates the relationship between the tolerance factor and the successful synthesis of several manganite and chromite perovskites, to give an updated perspective on these principles. This scatter plot, whether synthesis was achieved under nearly identical conditions or not, exemplifies a crucial concept about the interaction of crystal chemistry and synthesis feasibility. This information could be used as a semi-quantitative guideline for future solvothermal perovskite synthesis. It may also provide a useful starting point for simulations aiming at acquiring a better understanding of materials production processes.

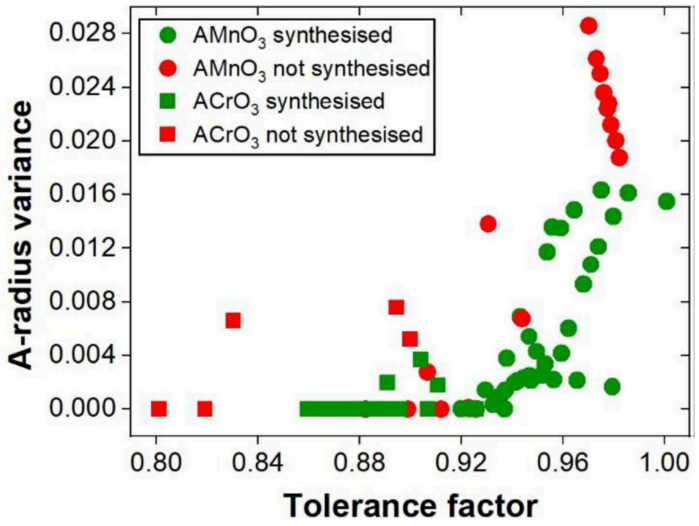


Figure 4. The plot of tolerance factor against radius of A-cation for $AMnO_3$ and $ACrO_3$ perovskites (reprinted from [89] with permission).

3.2. Hydrothermal Synthesis of $SrTiO_3$

It is established that the control of the shape and size distributions, as well as crystallinity, is normally superior in the hydrothermal condition compared to other synthesis methods [90–92]. This method has been used in the synthesis of $SrTiO_3$ nanoparticles.

Zhang et al. reported hydrothermal step-wise synthesis of $SrTiO_3$, which is depicted in Figure 5 [93]. They proposed a dissolution-precipitation mechanism for the synthesis of $SrTiO_3$. Some researchers have carried out the synthesis of $SrTiO_3$ by varying the hydrothermal conditions as shown in Table 1. The conventional hydrothermal reaction involves mixing the reactants with the appropriate solvent as the medium and heating the mixture in an autoclave at high temperatures.

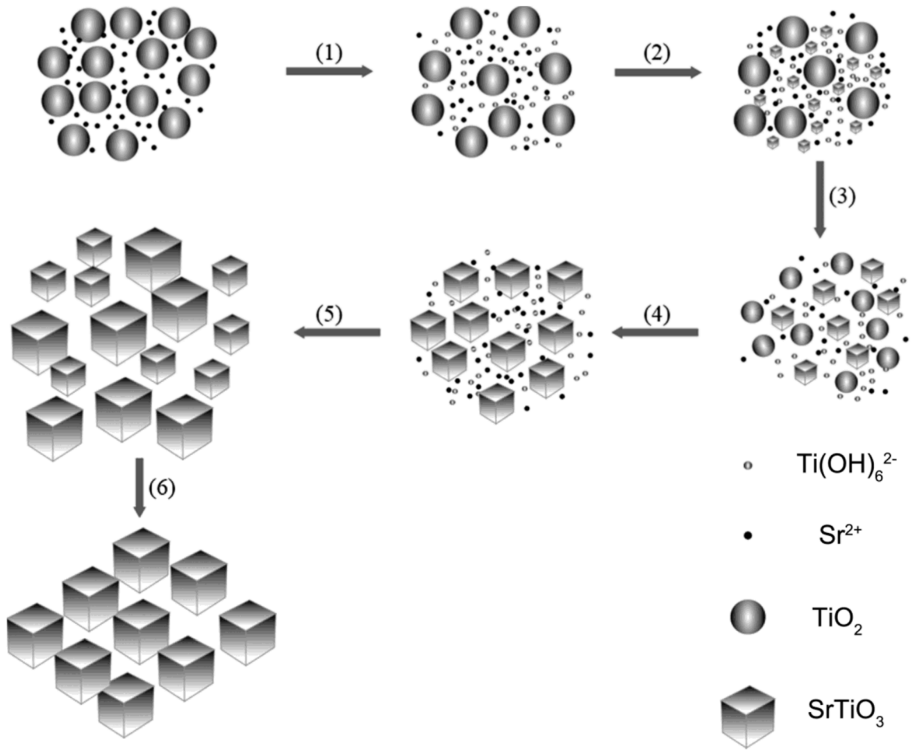


Figure 5. Hydrothermal synthesis of $SrTiO_3$ (Reprinted from [93] with permission).

Table 1. Hydrothermal conditions for the synthesis of $SrTiO_3$.

Sr Salt	Ti Salt	Medium	Time (h)	Temperature (°C)	Size (nm)	Reference
$Sr(OH)_2$	TiO_2	NaOH	1	180	10–100	[94]
$Sr(Ac)_2$	$Ti(OBu)_4$	Glycerol	-	240	20–200	[95]
$Sr(OH)_2{\cdot}8H_2O$	TiO_2	KOH	72	60–180	30–56	[96]
$Sr(OH)_2{\cdot}8H_2O$	TiO_2	-	12	180	20–50	[97]
$Sr(OH)_2{\cdot}8H_2O$	TiO_2	KOH	72	150	50	[98]
$Sr(OH)_2{\cdot}8H_2O$	TiO_2	NaOH	20–60	220	32–45	[93]
$SrCl_2{\cdot}6H_2O$	$C_{12}H_{28}TiO_4$	KOH	2.6	140	46–57	[92]
$Sr(OH)_2{\cdot}8H_2O$	TiO_2	NaOH	24	130	20–200	[99]
$Sr(OH)_2{\cdot}8H_2O$	$(C_6H_{20}N_2O_6)_2Ti(OH)_2$	NaOH	48	200	20–100	[100]
$Sr(OH)_2{\cdot}8H_2O$	TiO_2	NaOH	12	200	30–50	[101]

It has been observed that the alkaline medium is very important for the dissolution of TiO_2. Huang et al. reported that an increase in the synthesis temperature resulted in an increase in the size of the $SrTiO_3$ particles and a hydrothermal synthesis temperature of 130 °C was considered the optimum for the synthesis of $SrTiO_3$ [99]. They also established

that the synthesis duration may affect the particle size of $SrTiO_3$ nanoparticles, as this process is associated with Ostwald ripening, which includes both thermodynamic and kinetic aspects. Shen et al. attempted to synthesize $SrTiO_3$ without the use of an alkaline medium at various hydrothermal temperatures [102]. They reported that the irregular growth of the particles resulted in a heterogeneous microstructure. Zhang et al. proposed that the mole fraction of Sr/Ti significantly influences the surface area and the particles' sizes during the nucleation and crystal growth processes [93]. The reaction period should be shorter, while the mole fraction of Sr/Ti should be higher to obtain $SrTiO_3$ nanoparticles of a large surface area and smaller sizes. Alternatively, a longer reaction period and a lower mole fraction of Sr/Ti result in the formation of larger particles of $SrTiO_3$ with small surface area. In 2015, Mourão et al. reported the hydrothermal synthesis of $SrTiO_3$ nanoparticles, highlighting the effect of the mechanical stirring process [90]. During the hydrothermal reaction, the stirring effect increases the rate of collisions of the particles. It was found that the $SrCO_3$ phase was removed using mechanical stirring. Moreover, it was found that the samples of $SrTiO_3$ nanoparticles, which underwent stirring during the hydrothermal reaction, showed better photocatalytic activity compared to those samples that did not undergo stirring. Sometimes, hydrothermal reactions are coupled with microwave reactions, also known as microwave-assisted hydrothermal reactions. The coupling of microwave with hydrothermal reactions can be considered an exceptional method for nanomaterials synthesis. In 2012, Souza et al. used microwave hydrothermal synthesis to produce $SrTiO_3$ [92]. They observed that $SrTiO_3$ particles formed after 4 min of reaction. This resulted in a much shorter reaction time compared to conventional hydrothermal synthesis, which requires at least 1 h for the formation of $SrTiO_3$. The high-frequency microwave radiation is absorbed directly by the mixture, which contains permanent water dipoles, resulting in rapid heating due to molecular rotation. Therefore, microwave radiation can play an important role in increasing the rate of ion collision, thus promoting the nucleation of the $SrTiO_3$ phase. However, for nanoparticles of $SrTiO_3$, they have to go through different processes such as cluster formation, self-assembly, and crystal growth.

The enhanced photocatalytic efficiency of the microwave-hydrothermal treated $SrTiO_3$ is due to the combined effect of thermal and non-thermal processes of the microwave radiation on the nucleation process, ionic transport, and crystallite orientation growth. While the traditional hydrothermal heating is accomplished through wall-to-fluid heat conduction leading to temperature gradients of 15–40 °C in the autoclave vessel, microwave treatment results in volumetric heating of the aqueous solution of the precursor based on the dipole rotation of water molecules and ionic conductance loss of dissolved precursor ions, thus providing almost constant bulk temperature gradients in 2–5 min. Such quick and homogeneous heating leads to concurrent supersaturation in the entire reaction zone providing conditions of burst nucleation regime, featuring high nucleation rate and narrow size distribution of nuclei.

In addition to heating, the alternating electrical field applies non-thermal effects on charge-carrying precursors. The gradient of the field results in a dielectrophoretic force exerted on the polarized metal-oxo cluster, resulting in the orientation of the growth units. This process facilitates anisotropic growth due to a reduction in orientational entropy barrier for epitaxy on high-index facets. At the same time, the different surface polarization of crystallographic facets with different values of the dielectric loss factor leads to thermodynamic selectivity of facet-dependent growth and formation of crystal forms with catalytically active surfaces. Moreover, the fast quenching of the process under microwave power-off results in the high density of oxygen vacancies and polaron centers Ti^{3+} compared with the conventional hydrothermal product. Oxygen vacancy defects lead to the

formation of intra-gap states extending the absorption range into the visible region and acting as electron-trapping centers hindering electron–hole recombination.

3.3. Doping Strategies and Heterojunctions/Composite Materials

Doping of the $SrTiO_3$ crystal structure with aliovalent or isovalent metal cations at the sites of A (Sr^{2+}) and/or B (Ti^{4+}) through substitutional processes offers a highly effective approach to modify the electronic structure, band gap, and charge carrier behavior. This can be easily achieved during hydrothermal synthesis by adding a simple metal precursor to the reaction mixture. Doping of the Cr ions on the $SrTiO_3$ material was adopted by Yang et al. [103] through a one pot hydrothermal method. The doping was oriented on site B of the $SrTiO_3$ material in order to enhance its visible light absorption. Kato et al. [104] doped $SrTiO_3$ with Na^+ ions and found that Na^+ doping was able to reduce the energy bandgap. Wang et al. [105] described the doping of $SrTiO_3$ by the alkaline earth metal ions, such as Mg^{2+}, Ca^{2+}, and Ba^{2+} using the DFT-based calculation. Among the analyzed earth metal ions, Ba^{2+} was considered as the most efficient ion in effectively enhancing the photocatalytic activity of $SrTiO_3$. Wu et al. [98] developed a visible-light active Mn^{2+} doped $SrTiO_3$ photocatalyst via a single hydrothermal route. The formation of a new $Mn^{2+}/SrTiO_3$ heterojunction resulted in the narrowing of the energy bandgap and enhancing visible-light absorption. Ir-doped $SrTiO_3$ were synthesized using the one step hydrothermal approach and reported by Van et al. [106]. It has been proven from several experiments that iridium ions with valence 4+ and 3+ have been doped in $SrTiO_3$, thereby reducing the band gap and improving light absorption. Doping with a single non-metal element has also produced considerable attention in order to improve the ability to absorb visible light and photocatalytic activity. The non-metal elements may be incorporated into the $SrTiO_3$ lattice structure by the replacement of O^{2-} ions. In a study, Wang et al. [107] synthesized N-doped $SrTiO_3$ powder via the high-energy ball milling with $SrTiO_3$ and 20 wt% hexamethylene tetramine, urea, or ammonium carbonate, followed by high temperature calcinations. Such N-doping reduces the energy gap, enhancing visible light absorption and markedly increasing photocatalytic efficiency in NO decomposition. Hexamethylene tetramine, among all N-doping precursors, was proved to be the most suitable for the improvement in both specific surface area and photocatalytic activity. A study by Shan et al. [108] described the preparation of B-doped $SrTiO_3$ polyhedral nanosheets by the solid state method. The proper amount of B doping resulted in significant enhancement of photocatalytic performance of $SrTiO_3$ for CO_2 reduction.

Sun et al. showed successful fabrication of well heterojunction formation when $SrTiO_3$ with oxygen vacancies was constructed with $Cd_{0.5}Zn_{0.5}S$ (CZS) by using hydrothermal process [109]. XPS measurement illustrated contribution oxygen vacancies in heterojunction formation. A shift appeared for $SrTiO_3$/CZS nanocomposite in the direction of increasing the binding energy for S 2p, Zn 2p and Cd 3d peaks. Such a shift led to strong interaction between $SrTiO_3$ and CZS. Electronic, optical, and structural characteristics of MWCNT/Zr-doped $SrTiO_3$ heterojunction have been examined by means of DFT simulations [110]. The band gap of heterojunction is smaller than pure $SrTiO_3$ because of the interface effect occurring between $SrTiO_3$ and MWCNT. Smaller band gap values provided effective electron transferring from VB to CB and led to a wide visible light absorption range.

3.4. Equivalent and Hetero Valent Doping in $SrTiO_3$

Both the equivalent and hetero valent kind of dopants and its valence state in relation to the host ion control the photocatalytic performance of doped $SrTiO_3$. Dopants can therefore be divided into equivalent (isovalent) and hetero valent (aliovalent) dopants, each of which affects the electronic structure and defect chemistry in a different way. Isovalent

dopants, such Zr^{+}, Hf^{+}, and Sn^{+} at the Ti^{+} site or Ba^{2+} and Ca^{2+} at the Sr^{2+} site, preserve charge neutrality and mainly cause lattice distortions because of variations in ionic radius. Without causing appreciable defect concentrations, these distortions modify the lengths of Ti–O bonds and the orbital overlap between O 2p and Ti 3d states, leading to mild changes in the band structure and increased charge-carrier mobility [111,112]. As a result, while maintaining crystallinity and reducing recombination centers, isovalent doping typically enhances charge separation.

Hetero valent doping, on the other hand, substitutes ions of other valence states, such as La^{3+} in place of Sr^{2+}, Nb^{3+} in place of Ti^{+}, or Cr^{3+}, Rh^{3+}, Fe^{3+}, and Al^{3+} in place of Ti^{+}. Oxygen vacancies, cation vacancies, or modifications to the oxidation state of nearby ions must be created in order to compensate for the ensuing charge imbalance [113,114]. More than isovalent doping, these defects alter the electrical structure by introducing donor or acceptor energy levels within the band gap. In order to facilitate electron transport and increase hydrogen evolution activity, donor dopants like La^{3+} and Nb^{3+} contribute extra electrons and form shallow states close to the conduction band minimum. Cr^{3+} and Rh^{3+} produce interstate levels above the valence band, which in turn improve the solar-light absorption even in the visible range [115,116].

Oxygen vacancies creation is one of the important advantages of hetero valent atom doping. These oxygen vacancies can enhance interfacial charge transfer and decrease charge carrier recombination. The effective band gap can be narrowed by vacancy-induced defect states, which in turn generates internal electric fields that directs charge carriers towards active sites [117]. Also, high concentrations of oxygen vacancies can turn into recombination sites and reduce the photocatalytic efficiency. In order to attain the best possible balance between charge separation and carrier lifespan, precise management of defect concentration is necessary [118]. Charge separation and visible light absorption are improved by impurity states and moderate defect concentrations at low doping levels. However, lattice deformation, defect clustering, and enhanced recombination formed by increasing the dopant concentration over an optimum level, reduce the photocatalytic effectiveness [119]. According to the literature, depending on the dopants and synthesis techniques, the optimum concentration of aliovalent dopants is considered to be in between 0.5 and 5 mol%. While Cr- and Rh-doped $SrTiO_3$ have optimal visible-light photocatalytic efficiency at concentrations below 2 mol%, La-doped $SrTiO_3$ exhibits improved hydrogen-evolution activity in the range 1–3 mol% La [115,120]. These findings emphasize how crucial it is to balance defect management and band-gap engineering when creating high-performance $SrTiO_3$ photocatalysts. While hetero valent doping integrates band-gap engineering, oxygen-vacancy creation, and defect-mediated charge separation, equivalent doping mainly increases photocatalytic activity by lattice modification and improved carrier transport. To maximize the photocatalytic efficacy of $SrTiO_3$-based materials, these parameters must be optimized synergistically [112,114,117].

4. Photocatalytic Water Remediation

Among viable alternatives to fossil fuels, solar energy stands out as the most popular choice on a global scale. Its abundance, environmental friendliness, and inexhaustible supplement is responsible for its widespread use. According to estimates by the EIA [121], the world consumes about 600 EJ (1 EJ = 1018 joules) of energy every year, and by 2040, this number is predicted to increase to 750 EJ. On the other hand, Earth receives approximately 4,000,000 EJ of solar energy each year, of which only 50,000 EJ efficiently used [122]. By using just, a portion of this enormous solar energy resource's potential, it is possible to significantly reduce the amount of energy needed to meet global energy demands. In addition to photovoltaics, photocatalytic techniques, such as turning CO_2 into CO and CH_4

fuels [123] or the splitting of water to H_2 fuel [124], also play a critical part in the harvesting of solar energy. Even though these strategies demonstrated potential, it is still difficult to fully attain the required efficiency for commercial viability.

Meeting the worldwide challenge of water accessibility imposes the need to diversify from traditional water treatment methods to other harmonizing methods in order to find a sustainable solution. Traditional water treatment technologies, such as adsorption and filtration, are inadequate in purifying water which is contaminated with chemically stable substances such as organic solvents, organic dyes, and pharmaceuticals [125]. The urgency of reducing clean water supplies and the fast industrialization-related contamination of already-existing water sources have greatly increased the significance of wastewater recycling. Organic dyes are a major source of wastewater contamination, accounting for approximately 15% of the dyes used in the textile sector [126]. The growing presence of antibiotics and medicines in water sources shows major threats to human health [127,128]. An alternative to these problems is to use photocatalytic oxidation, a technique that can completely mineralize these organic contaminants [129,130]. This method has a lot of potential for addressing the immediate and challenging issue of organic pollutant removal during wastewater treatment. Having said that, these perovskite materials can be promising agents to be used in developing alternative water treatment technologies. This material performing advanced oxidation process can be the promising agent for the removal of organic pollutants from wastewater by generating hydroxyl radicals as oxidizing species, which leads to the possible mineralization and degradation of organic pollutants.

The initiation of redox reactions in photocatalysis is caused by the excitation of valence electrons to the conduction band which is initiated by solar irradiation as shown in Figure 6. This excitation results in the formation of electron–hole pairs, which then travel across the surface of the catalyst, promoting reduction and oxidation reactions either directly or indirectly [131,132]. The positively charged holes produced can either directly or indirectly oxidize contaminants by producing $^{-}$OH radicals. Conversely, electrons in the conduction band contribute to the reduction in adsorbed oxygen [5,133]. It is worth noting that electron–hole pair recombination is a barrier to the photocatalytic process. To inhibit recombination, the presence of electron scavengers such as oxygen is essential. When oxygen molecules are adsorbed, they can scavenge electrons and produce a superoxide radical (O_2^{-}). This superoxide radical can then be protonated, resulting in the creation of a hydroperoxyl radical ($HO^{\bullet}$) and, eventually, hydrogen peroxide (H_2O_2). The intricate interaction of electron and hole movements illustrates the complex, yet fascinating mechanisms involved in photocatalytic redox processes. A suitable photocatalyst for such applications must be visible-light active, allowing for the use of a wider range of the solar spectrum [134]. To withstand potential corrosion caused by photogenerated oxidant species, the material must have exceptional chemical stability. Furthermore, a high degree of crystallinity is extremely desirable because it tends to improve catalytic activity. This improvement can be due to the elimination of surface imperfections of the material, which frequently operate as charge carrier traps or recombination centers [135]. Furthermore, lowering particle size is an interesting method to investigate because it can effectively limit recombination by shortening the diffusion path-length for charged particles. Finally, a large surface area is an important issue because it frequently results in improved activity by enhancing active sites.

TiO_2 has emerged as the material of choice for photocatalytic applications since the early 1970s. This universal preference is due to its ample supply, outstanding stability, and the benefit of a configurable band gap [136]. Nonetheless, despite its high efficacy, TiO_2 has several limits. One significant drawback is TiO_2's tendency for rapid charge carrier recombination, which can reduce the overall effectiveness of the photocatalytic process. There is also the possibility of nonstoichiometric H_2/O_2 generation due to TiO_2 self-

oxidation [137,138]. Furthermore, TiO_2, similar to other photocatalysts, has the constraint of only absorbing the ultraviolet component of solar irradiation, which accounts for around 5% of total sunlight that reaches the Earth [139]. These aspects highlight the need for ongoing study and innovation in the field of photocatalysis, with the goal of overcoming the constraints and realizing the full potential of photocatalytic materials in harvesting solar energy for a variety of applications.

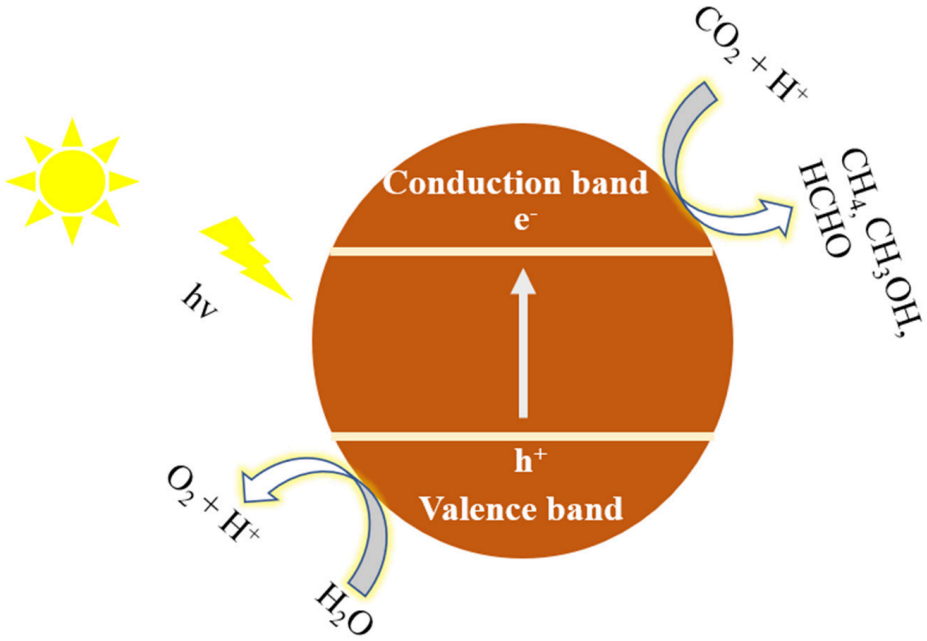


Figure 6. Excitation process of a semiconductor under light irradiation.

Perovskite oxides have emerged as extremely attractive candidates for photocatalysis, due to their extraordinary range in terms of composition and electrical structure, which allows for easy band gap engineering. Specifically, titanate and tantalate-based perovskite oxides have shown strong photocatalytic efficacy in a variety of investigations [140–145]. Among these, $SrTiO_3$-based perovskite oxides are promising, especially when exposed to UV irradiation, because they display good photo-corrosion resistance and structural stability [146,147]. While natural $SrTiO_3$ predominantly responds to UV light, the ability to change its characteristics represents a breakthrough. It is feasible to generate a reaction in visible light and increase overall photocatalytic activity by strategically introducing appropriate ions at specified cationic or anionic sites via doping. This is achieved by narrowing the band gap of $SrTiO_3$ [116,148,149]. These developments raise the prospect of enhancing the utility of perovskite oxides in photocatalysis, particularly in harnessing the potential of visible light for a variety of applications.

A considerable improvement in visible light responsiveness is seen in Figure 7, which was accomplished by elevating the top of the valence band using a 0.5 mol% B-site doping method. This impact is especially noticeable for specific elements, such as Mn, Rh, Ru, and Ir [150]. Furthermore, the decrease in band-gap for $Sr_{0.66}Zn_{0.33}TiO_3$ has been successfully verified. This decrease is attributed to the formation of additional Zn 2p energy levels at the conduction band's lower end [151]. In a recent study, Li et al. reported a solvothermal technique to synthesis Fe-doped $SrTiO_3$ nanoparticles [152]. The addition of Fe^{3+} substituents led to a significant narrowing in the band gap. When tetracycline was degraded under visible light irradiation, the conversion efficiency increased 14-fold compared to the undoped $SrTiO_3$ sample with 3 mol% Fe-doped $SrTiO_3$. Introduction of F [153] and N [154,155] at the anionic sites has improved the photocatalytic performance in organic dye removal.

This improvement is related to increased electron mobility and the production of Ti^{3+} ions, which have a high absorption capacity for visible light [156]. These findings highlight the possibility of doping techniques to improve photocatalytic performance, particularly in the setting of visible light-driven reactions, providing promising options for future research.

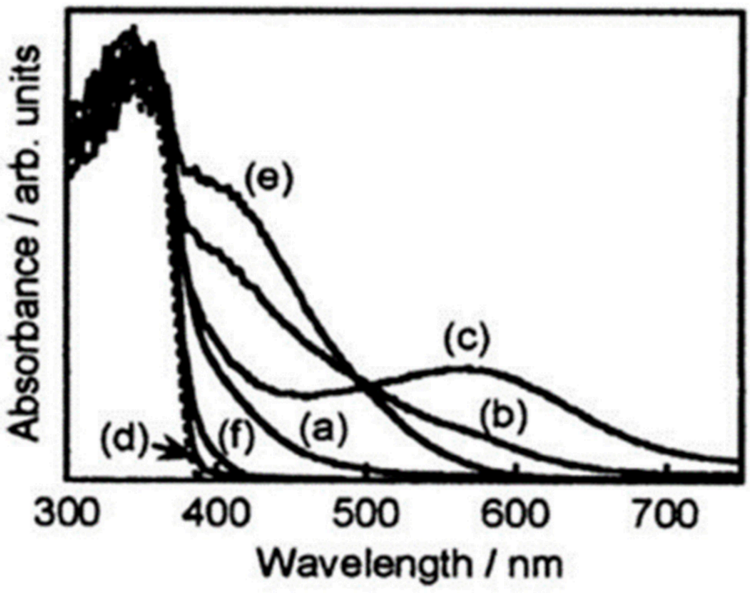


Figure 7. UV-Vi's absorbance spectra of $SrTiO_3$ with dopants (a) Mn, (b) Ru, (c) Rh, (d) Pd, (e) Ir, and (f) Pt (reprinted from [116] with permission).

Despite significant advances in perovskite oxide catalysts, their efficiency in the photocatalytic degradation of organic pollutants still falls short when compared to noble metal catalysts, such as Pd/CeO_2-Al_2O_3 [157] and Au/CeO_2 [158]. The complex interactions between the metal and the support produce various catalytic characteristics in such systems. The interactions between electrical and ionic forces among the metal and the support play a crucial role in increasing catalytic activity [159–163]. They help in stabilizing the oxidation state of the active phase [164–168] and provide resistance to sintering [169–172]. These findings highlight the distinct advantages of supported metal catalysts and highlight the necessity for additional modification of perovskite oxide catalysts, which make them suitable for different applications. The preferred support materials are chemically and thermally stable mesoporous substrates with a large surface area. These characteristics are purposefully chosen to ensure excellent dispersion and reactivity of metal sites [3], resulting in increased contact areas and easy access to reactants [20,173]. There is limited research available in the literature on perovskite oxide-supported metal catalysts. This research gap can be related to the difficulties in synthesizing pure-phase, multi-component perovskite oxides with high porosity.

4.1. Photocatalytic Mechanism of Pristine $SrTiO_3$

Because of its superior chemical stability, strong resistance to photocorrosion, and appropriate electronic structure for redox reactions, $SrTiO_3$ is one of the perovskite oxide photocatalysts that has been studied the most. Because of its large band gap (~3.2 eV), pristine $SrTiO_3$'s photo response is mainly restricted to the ultraviolet, which makes up a very small portion of the solar spectrum. Electron–hole pairs (e^-/h^+) are produced when UV light excites electrons from the O 2p-derived valence band to the Ti 3d-derived conduction band [133,174–176]. While conduction-band electrons convert liquid oxygen to become superoxide radicals ($O_2\bullet^-$), photogenerated holes react with surface hydroxyl groups or adsorbed water molecules to produce hydroxyl radicals (•OH). The breakdown

of organic contaminants and the stimulation of photocatalytic redox processes are caused by these reactive oxygen species [174–176]. Charge carrier recombination and insufficient visible light absorption reduce the efficiency of the photocatalytic process, which in turn limits the practical photocatalytic efficiency of pristine $SrTiO_3$ [175,176]. A summary of some important works of pure $SrTiO_3$ materials and their photocatalytic applications is given in Table 2.

Table 2. Summary of photocatalytic activities of pristine $SrTiO_3$ materials reported in the literature.

Catalyst Type	Synthesis Conditions (Temp./Precursors/Time)	Photocatalyst Conc.	Target Molecule & Conc.	Irradiation Type	Efficiency/Time	Ref.
$SrTiO_3$ nanoparticles (polyhedral)	Hydrothermal; 120 °C; SrO + $Ti(OC_4H_9)_4$ + Ethanolamine; 36 h	1.0 g/L	MO, 10 mg/L	UV (500 W Hg lamp, λ = 384 nm)	92.3% degradation/240 min	[102]
$SrTiO_3$ nanocubes	Hydrothermal; 130 °C; $Sr(OH)_2{\cdot}8H_2O$ + P25-TiO_2 + NaOH; 72 h	0.5 g/L	CV, 10 mg/L	UV (15 W lamp, λ = 365 nm)	99% degradation/24 h	[99]
$SrTiO_3$ nanocubes (porous, self-assembled)	Hydrothermal; 200 °C; $Sr(NO_3)_2{\cdot}5H_2O$ + $Ti(SO_4)_2$ + KOH; 8 h	0.2 g/L	RhB, 10 mg/L	UV (300 W Xe lamp)	96% degradation/360 min	[177]
$SrTiO_3$ hollow microspheres	Hydrothermal; 180 °C; $SrCl_2$ + $Ti(OBu)_4$ + NaOH; 6 h	1.0 g/L	Cr(VI), 30 mg/L	300 W Xe lamp	90% reduced/120 min	[178]
Porous $SrTiO_3$ spheres	Hydrothermal; 150 °C; $SrCl_2$ + Titanate + NaOH; 72 h	~1.0 g/L	RhB, 2×10^{-5} mol/L	UV (λ = 254 nm)	100% degradation/20 min	[179]
$SrTiO_3$ nanoflowers (hierarchical)	Hydrothermal; 160 °C; $Sr(NO_3)_2$ + Tetrabutyl titanate + NaOH; 24 h	10.0 g/L	RhB, 5 mg/L	UV (24 W lamp, λ = 365 nm)	~50% degradation/180 min	[180]
$SrTiO_3$ single crystals	Hydrothermal; 180 °C; $Sr(NO_3)_2$ + $Ti(OBu)_4$ + NaOH + Ethanolamine; 24 h	~0.5 g/L	H_2/O_2 evolution	UV (300 W Xe lamp)	H_2: 71.1 µmol/h; O_2: 30.0 µmol/h	[181]
Intrinsically activated $SrTiO_3$ (noble-metal-free)	Activated in H_2 700 °C, 4 h	0.2 g/L	H_2 evolution (MeOH/H_2O)	UV (300 W Xe)	Up to 0.15 µmol/h H_2 (no cocatalyst)	[182]

4.2. Photocatalytic Mechanism of Doped $SrTiO_3$

One of the techniques to improve the performance of $SrTiO_3$ is elemental doping. Adding metal or non-metal dopants to the $SrTiO_3$ lattice increases the localized energy states within the band gap, improving the light absorption into the visible region and enhancing charge carrier separation [115,183–185]. Fe, Mn, Rh, Ru, Ir, and Pt are examples of transition metal dopants that can replace Ti sites and provide intermediate electronic states that lower $SrTiO_3$'s effective band gap [183,184]. As a result, photo generated carrier generation increases, and visible-light absorption is enhanced. Further, the creation of impurity levels improves the charge transfer while inhibiting charge carrier recombination causes Fe-doped $SrTiO_3$ to show noticeably enhanced photocatalytic activity [184].

Similarly, it has been demonstrated that anion doping with nitrogen and fluorine alters the valence band structure by introducing N 2p states and producing Ti^{3+} species and oxygen vacancies [185,186]. These changes extend charge carrier lifetimes, boost carrier mobility, and enhance visible light absorption. Dopants frequently serve as trapping centers for photogenerated electrons or holes in addition to narrowing the band-gap. This reduces recombination and increases the availability of charge carriers for surface photocatalytic reactions. For applications such as CO_2 reduction, hydrogen production, and pollutant degradation, doped $SrTiO_3$ typically shows better photocatalytic activity than pure $SrTiO_3$ [115,183–186]. A summary of some doped $SrTiO_3$ materials with their photocatalytic applications is given in Table 3.

Table 3. Summary of photocatalytic performance of doped $SrTiO_3$ materials.

Catalyst Type	Synthesis Conditions (Temp./Precursors/Time)	Photocatalyst Conc.	Target Molecule & Conc.	Irradiation Type	Efficiency/Time	Ref.
Mn^{2+}-doped $SrTiO_3$ nanocubes	Hydrothermal; 150 °C; $MnCl_2{\cdot}4H_2O$ + $Sr(OH)_2{\cdot}8H_2O$ + TiO_2 + KOH; 72 h	1.0 g/L	Tetracycline (TC), 10 mg/L	Visible (λ > 420 nm, 300 W Xe)	66.7% degradation/ 60 min (5 at% Mn)	[98]
N-doped $SrTiO_3$	Solvothermal; 200 °C; $Sr(NO_3)_2{\cdot}4H_2O$ + $Ti(OC_3H_7)_4$ + KOH; 3 h	1.0 g/L	MO, 0.005 g/L	40 W mercury lamp and xenon lamp	~99% degradation/ 120 min	[154]
Cr-doped $SrTiO_3$	Solvothermal; 200 °C; $Cr(NO_3)_3{\cdot}9H_2O$ + $Sr(NO_3)_2$ + $(C_4H_9O)_4Ti$ + NaOH; 12 h	1.0 g/L	Cr(VI), 10 mg/L	Visible (λ > 420 nm, 300 W Xe)	92% Cr(VI) reduction/210 min (0.9 at% Cr)	[103]
La,Cr co-doped $SrTiO_3$	Sol–gel hydrothermal; 180 °C; $La(NO_3)_3$ + $Cr(NO_3)_3$ + $Sr(NO_3)_2$ + Titanium tetra-isopropoxide; 36 h	0.5 g/L	H_2 + O_2 (overall water splitting)	Visible (λ > 420 nm, 300 W Xe)	H_2: 9.1 µmol/h; O_2: 2.4 µmol/h/10 h;	[187]
Al-doped $SrTiO_3$	Fluxed method; $SrTiO_3$ + Al_2O_3, 1100 °C, 10 h	1.0 g/L	Overall water splitting (H_2 + O_2)	UV (300 W Xe, λ > 300 nm)	H_2: 550 mmol/h O_2 = 280 mmol/h	[138]
Bi-doped $SrTiO_3$	Solid-state; 750 °C; Bi_2O_3 + $SrCO_3$ + TiO_2; 24 h	0.5 g/L	AO7 (acid orange 7), 10 mg/L	Visible (300 W)	95.8% degradation/ 120 min	[188]
La-doped $SrTiO_3$ porous microspheres	Modified sol–gel + Agarose template; 1000 °C; La_2O_3 + $SrCO_3$ + TiO_2; 10 h	1.0 g/L	Cr(VI), 10 mg/L	Visible (λ > 400 nm, 300 W Xe)	84% Cr(VI) reduction/100 min	[189]
N-doped $SrTiO_3$ nanoparticles	Solvothermal; 200 °C; $Sr(NO_3)_2$ + $Ti(OC_3H_7)_4$ + KOH; 3 h	0.6 g/L	Cr(VI), 5 mg/L	300 W mercury lamp (λ ≥ 400 nm)	~100% Cr(VI) reduction/120 min	[190]
Bi-doped $SrTiO_3$	Hydrothermal; 200 °C; $Bi(NO_3)_3$ + $Sr(NO_3)_2$ + Tetrabutyl titanates + NaOH; 24 h	0.3 g/L	CO_2 reduction → CO + CH_4	Visible (λ > 420 nm, 300 W Xe)	CO: 5.58 µmol g^{-1} h^{-1}; CH_4: 0.36 µmol g^{-1} h^{-1}	[191]
Cr-doped $SrTiO_3$	Co-precipitation; 900 °C calcination; $Cr(NO_3)_3$ + $Sr(NO_3)_2$ + TiO_2; 4 h	1.0 g/L	MB, 10 mg/L	Visible (λ > 420 nm, 300 W Xe)	88% MB degradation/ 120 min	[192]

4.3. Photocatalytic Mechanism of $SrTiO_3$-Based Heterostructures

By forming composites with other semiconductors, noble metals and corban-based materials $SrTiO_3$ can form heterostructures and can mitigate the challenge of carrier recombination [193–196]. An internal electric field is created at the interface when a heterojunction forms, encouraging directional charge transfer and improving charge separation effectiveness.

In traditional Type-II heterojunctions, holes go in the opposite direction of electrons, which migrate from a semiconductor with a greater conduction band potential to one with a lower band potential. By this spatial separation of charge carriers, catalytic efficiency is improved by reduced recombination [193,194]. Z-scheme heterojunctions also preserve robust redox capacity which in-turn increases the charge separation efficiency by conserving reduced electrons and oxidized holes [194,195].

A further substantial group of photocatalyst material is metal-semiconductor heterostructures. As noble metals like Au, Ag, Pt, and Pd form hetero structures with $SrTiO_3$, producing Schottky junctions, these metals functions as an electron sink, by absorbing photogenerated electrons and reducing recombination losses [195,196]. Furthermore, combining $SrTiO_3$ with graphene or graphene oxide generates conductive electron transport channels that increase the charge carrier mobility and enhances photocatalytic activity [197,198]. Hence, $SrTiO_3$-based materials and heterostructure engineering is one of the most capable methods for optimizing usage and improving the photocatalytic performance. Table 4 provides photocatalytic applications of some $SrTiO_3$ based heterostructure materials.

Table 5 provides a concise summary of key photocatalysts along with the elements employed for doping, the corresponding variations in their band gap, the observed photocatalytic efficiency, and their specific practical applications, as discussed in the preceding section.

Table 4. Summary of photocatalytic performance of $SrTiO_3$-based heterostructure materials.

Catalyst Type	Synthesis Conditions (Temp./Precursors/Time)	Photocatalyst Conc.	Target Molecule & Conc.	Irradiation Type	Efficiency/Time	Ref.
$Fe_2WO_6/SrTiO_3$	Hydrothermal; 200 °C; $Fe(NO_3)_3$ + Na_2WO_4 + $Sr(NO_3)_2$ + Titanium butoxide + NaOH; 16 h	0.5 g/L	RhB, 5 mg/L	Visible (150 W)	96.1% degradation/120 min	[199]
$SiTiO_3/NiFe_2O_4$	Sol–gel; 110 °C; $NiCl_2$ + $FeCl_3$ + $SrCl_2$ + $(CH_3CH_3CHO)_4Ti$; 12 h	1.0 g/L	RhB, 20 mg/L	Simulated solar light	94.7% degradation/120 min	[200]
$SrTiO_3/ZnO$	Solvothermal; 200 °C; Tetrabutyl titanate + $Sr(Ac)_2$ + $Zn(Ac)_2$ + NaOH; 12 h	0.1 g/L	MO, 5 mg/L	Visible (300 W Xe)	48.8% degradation/60 min	[201]
$BiOI/SrTiO_3$	Electrospinning method; 900 °C, $Bi(NO_3)_3$ + $Ti(OC_4H_9)_4$ + $Sr(CH_3COO)_2$; 2 h	0.8 g/L	MO, 40 mg/L	Visible (250 W metal halide lamp)	94.6% degradation/180 min	[202]
$SrTiO_3/ZnIn_2S_4$	Oil-bath method; Tetrabutyl titanite + Zn $(Ac)_2$ + Sr $(Ac)_2$	0.1 g/L	MO, 10 mg/L	UV (300 W Xe)	97% degradation/32 min	[203]
$SrTiO_3/MnFe_2O_4$	MW hydrothermal; $Fe(NO_3)_3$ + $Mn(NO_3)_2$+ $Sr(OH)_2{\cdot}8H_2O$ + TiO_2	1.0 g/L	TC, 22 mg/L	300 W MW-UV	100% degradation/20 min	[204]
$SrTiO_3$/*g*-C_3N_4/ZnO	Wet impregnation and ultrasonic	0.65 g/L	TC, 28.24 mg/L	Visible light	96% degradation/72 min	[205]
g-$C_3N_4/SrTiO_3$	Sonication mixing	0.2 g/L	MB, 5 mg/L	Visible light irradiation ($\lambda > 400$ nm) LED flood lamps	~100% degradation/180 min	[206]
$SrTiO_3/Ti_3C_2T_x$	Hydrothermal	1.0 g/L	TCH, 10 mg/L	Visible light	~100% degradation/5 min	[207]
$SrTiO_3$ anchored rGO/*g*-C_3N_4	Wet impregnation; $SrCl_2$ + $C_{12}H_{28}O_4Ti$ + Melamine	1.0 g/L	MB + RhB, 10 mg/L	UV–Vis light irradiation (500 W Halogen lamp)	96% for MB dye and 34% for RhB dye degradation/100 min	[208]

Table 5. Photocatalytic water remediation by $SrTiO_3$.

Photocatalyst	Doping Element	Applications	Reference
$SrTiO_3$	None	UV-driven photocatalysis	[146,147]
$SrTiO_3$	Mn, Ru, Rh, Ir	Visible-light photocatalysis	[148]
$Sr_{0.66}Zn_{0.33}TiO_3$	Zn	Visible light photocatalysis	[151]
$SrTiO_3$	Fe (3 mol%)	Visible-light degradation of antibiotics	[153]
$SrTiO_3$	F, N	Organic dye degradation	[154–156]
Mn-$SrTiO_3$	Mn	Degradation of tetracycline	[98]
$SrTiO_3$	None	Degradation of crystal violet	[99]
mp N-$SrTiO_3$	N	Degradation of methyl orange	[209]
$BiVO_4/SrTiO_3$	None	Degradation of sulfamethoxazole	[210]
Ag, F-$SrTiO_3$	F	Degradation of VOCs (Toluene)	[211]
$TiO_2/SrTiO_3$ and $SrTiO_3$ microspheres	Rh, Ru, Pt	Phenol oxidation and degradation	[212]
Ag/Fe_3O_4 bridged $SrTiO_3$/GCN	None	Degradation of levofloxacin	[213]
Polythiophene/mp $SrTiO_3$		Degradation of methylene blue	[214]
Bimodal-pore $SrTiO_3$ microspheres		Cr (VI) removal	[215]

5. Photocatalytic Water Splitting

The photocatalytic hydrogen production is recognized as an eco-friendly approach for the creation of alternative green energy sources, considering that the reaction is simple and involves no emissions. In this case, $SrTiO_3$ acts as a photocatalyst, in which there is a redox

reaction due to the presence of photogenerated electron–hole pairs. Liu et al. conducted a study to examine the water-splitting efficiency of $SrTiO_3$ when exposed to strong UV light [22]. Later, Iwashina and Kudo were successful in splitting water when $SrTiO_3$ was doped with Rh, even in visible light [216]. After their study, the doping of $SrTiO_3$ was found to be of interest to other researchers. They synthesized Rh-doped $SrTiO_3$ under visible light irradiation, which was deposited onto a transparent indium tin oxide (ITO) electrode. Rh-doped $SrTiO_3$ has visible light absorption bands, which are absent in pure $SrTiO_3$. The electronic transition at 400 nm is attributed to transitions from the electron donor level of Rh^{3+} to the conduction band of $SrTiO_3$, whereas the electronic transition at 600 nm is attributed to transitions from the valence band (VB) of $SrTiO_3$ to the acceptor level of Rh^{4+}. Ham et al. studied the photocatalytic properties of Al-doped $SrTiO_3$ and the impact of $SrCl_2$ flux treatments in an alumina crucible [138]. The results showed that the flux acts as a medium for the dissolution of the dopant Al_2O_3, where the efficiency of the photocatalytic activity of the Al-doped $SrTiO_3$ is significantly high with an apparent quantum efficiency of over 30% at 360 nm, compared with $SrTiO_3$. The efficiency of the Al-doped $SrTiO_3$ is significantly high for the splitting of water, with 550 H_2 μmol h^{-1} and 280 O_2 μmol h^{-1}, where the $SrCl_2$ flux treatment is used for the preparation of $SrTiO_3$. Doping of the materials has significantly contributed to the improvement of photocatalytic materials by activating them in the visible light spectrum. Goto et al. have observed the photocatalytic activity of the microparticles of Al-doped $SrTiO_3$ with $Rh_{2-y}Cr_yO_3$ for the splitting of water with an apparent quantum yield of 56% at 365 nm and solar hydrogen conversion efficiency of 0.4% [217].

R. Asai et al. have prepared Rh and Sb-doped $SrTiO_3$, which was loaded with IrO_2 (IrO_2/$SrTiO_3$: Rh and Sb) [218]. The one-step photoexcitation system of IrO_2/$SrTiO_3$: Rh (0.5%) and Sb (1.0%) exhibited photocatalytic activity under visible light. Additionally, various cocatalysts such as RuO_2, Ru, and IrO_2 have also been used for water splitting with $SrTiO_3$: Rh (0.5%) and Sb (1.0%), and stoichiometric quantities of H_2 and O_2 gases have been produced from water. IrO_2 was found to be the best cocatalyst with H_2 evolution rates of 26 mL h^{-1} and O_2 evolution rates of 13 mL h^{-1} with $SrTiO_3$: Rh and Sb. In contrast, the non-loaded photocatalyst was found to be inactive for H_2 evolution with an AQY of merely 0.1% at 420 nm. The DRS measurement revealed that water splitting was accompanied by the transition from the Rh^{3+} donor levels to the conduction band of $SrTiO_3$ in the visible light range at λ = 500 nm.

Lyu et al. used the flux method to dope Al into $SrTiO_3$. The photocatalyst was loaded with $RhCrO_x$ cocatalyst by the diffusion-calcination method and considered as the best photocatalyst for the overall water splitting reaction with an AQY of 56% at 365 nm in the UV range [219]. Cobalt species was incorporated in $RhCrO_x$/$SrTiO_3$: Al through the photodeposition method using $CoCl_2$ for oxygen evolution in the process of hole extraction. This was intended for the reduction in oxidative corrosion of Cr^{3+} species through the utilization of the excess holes produced in the process. In this study, the incorporation of 0.3 wt% Co in $RhCrO_x$/$SrTiO_3$: Al exhibited stable photocatalytic activity of 5.7 μmol h^{-1}, which further reduced with increasing Co content up to 0.5 wt%. The presence of the photoexcited holes enhances the oxidation of water and $RhCrO_x$, resulting in the dissolution of Cr^{6+} in the absence of the CoOOH cocatalyst, which triggers the backward reaction in Cr-deficient $RhCrO_x$. Consequently, a loading effect is experienced on the oxidation sites, which leads to a build-up of photo-excited holes. The holes are mainly used to react with water, leading to oxidative corrosion of $RhCrO_x$. This leads to a suppression of the photocatalyst.

The water splitting reaction has been shown by Niishiro et al. using the Ru or Pt-loaded $SrTiO_3$: Rh system for the evolution of hydrogen (H_2) and the $BiVO_4$ group for

the evolution of oxygen (O_2) under visible light irradiation, with Fe^{3+}/Fe^{2+} being used as the mediators [220]. The electrons and holes generated by the visible light irradiation were used to reduce water into hydrogen gas and oxidize water into oxygen gas in the Rh-doped $SrTiO_3/Ru/BiVO_4$ system. Another $SrTiO_3$: Rh/Sb photocatalyst was prepared by the hydrothermal method by the same research group for the evolution of hydrogen and oxygen under visible light irradiation [139]. It has been observed that the highest rate of H_2 production is obtained when $SrTiO_3$ is doped with Rh, while the rate of O_2 evolution is enhanced when the Rh^{3+} ions are stabilized through the co-doping of $SrTiO_3$ with Sb, which prevents the formation of undesirable Rh^{4+} ions and oxygen defects.

Guan et al. prepared $SrTiO_3/Ag_3PO_4$ composite via hydrothermal processes with the use of $Sr(NO_3)_2$ and $AgNO_3$ [221]. In this case, $SrTiO_3$ was loaded into Ag_3PO_4 due to fast excitation and preservation by photoexcited electrons of $SrTiO_3$ in the visible light range. In addition, incorporation of $SrTiO_3$ increased oxygen generation by Ag_3PO_4 since $SrTiO_3$ behaved as a cocatalyst. In this study, $SrTiO_3/Ag_3PO_4$ composite with molar ratio of 1/20 had an initial rate of 1316 μmol h^{-1} and AQY of 16.2% for O_2 production (Figure 8a). The photocatalytic activity of physical mixing of different molar ratios of $SrTiO_3$ and Ag_3PO_4 was shown in (Figure 8b). In this case, the molar ratio of 1/5 was found to improve the O_2 evolution, but not so effectively because of low contact between $SrTiO_3$ and Ag_3PO_4. It is clear that doping of $SrTiO_3$ and interface contact between two photocatalysts will increase photocatalytic activity.

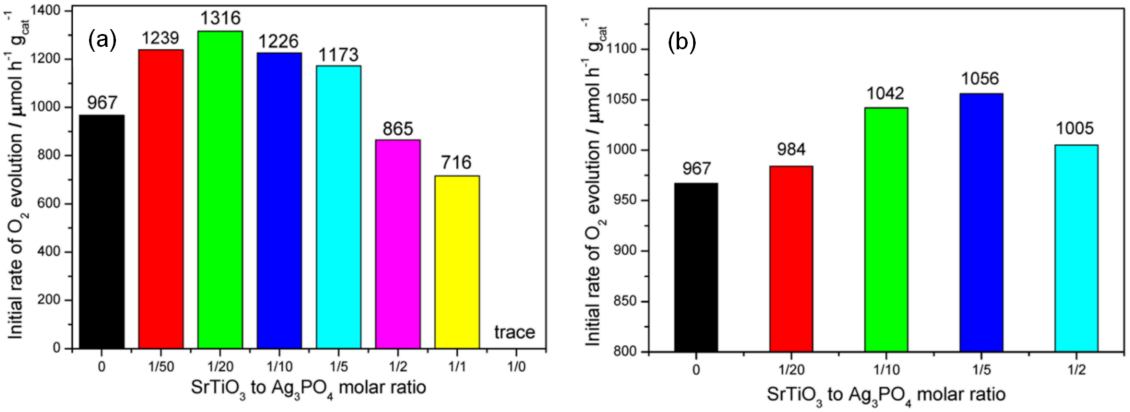


Figure 8. (**a**) Photocatalytic activity of $SrTiO_3/Ag_3PO_4$ composites with different molar ratios, (**b**) Photocatalytic activity of physical mixture of $SrTiO_3$ and Ag_3PO_4 with different molar ratios (Reprinted from [221] with permission).

6. Reactive Oxygen Species (ROS) Formation During $SrTiO_3$-Based Photocatalysis

The mechanisms involved in ROS production form the fundamental principles behind $SrTiO_3$-based photocatalytic systems which determine their efficiency towards environmental purification as well as for splitting water. Even though there is abundant information available regarding $SrTiO_3$ photocatalysis, the important issue remains unresolved to date in terms of a comprehensive, mechanistic analysis of how electrons (e^-), holes (h^+), superoxide anions ($O_2\bullet^-$), and hydroxyl radicals (•OH) are produced, modified, and released [222].

$SrTiO_3$ is an ABO_3 type perovskite semiconductor with a band gap ranging from about 3.2 eV to 3.4 eV along with suitable band edges for water splitting. The negative value of conduction band is thermodynamically capable of reducing oxygen to superoxide ($O_2\bullet^-$), i.e., −0.33 V vs. NHE. On the other hand, positive value of valence band makes $SrTiO_3$ competent for direct water oxidation and production of hydroxyl radical [223]. However,

thermodynamically permissible processes do not assure kinetic feasibility of a process, and the yield and nature of ROS depend on several factors including surface chemistry, defect concentration, co-catalyst loading, and environment of photocatalysis. Upon irradiation of photons having energy above the band gap, electrons get excited from valence band to conduction band, resulting in formation of electron–hole pairs.

The one-electron reduction in dissolved O_2 by conduction band electrons is the primary route to superoxide radical anion generation:

$$O_2 + e^-CB \rightarrow O_2\bullet^- \ (E^\circ = -0.33 \text{ V vs. NHE}) \quad (2)$$

The energy driving force for the above reaction lies in the high negative potential of the conduction band of $SrTiO_3$ (~0.5 V vs. NHE). Kinetic limitations can hinder the generation of $O_2\bullet^-$ when there is a lack of efficient co-catalysts or surface modification. There are reports of high $O_2\bullet^-$ generation upon incorporation of Pt or MnO_2 nanoparticles due to fast electron transfer from the semiconductor to the metals. Importantly, $O_2\bullet^-$ detection in the vast majority of photochemical experiments is done by indirect means with the use of colorimetric detection by EPR spin trapping using DMPO. Wang et al. showed by electron paramagnetic resonance (EPR) spin trapping utilizing DMPO [224]. DMPO-EPR has been regarded as the most reliable method of detecting $O_2\bullet^-$; however, the method needs to be properly controlled to avoid interference from DMPO oxidation products or •OH-induced DMPO-OH adducts [225].

The disproportionation drops from $O_2\bullet^-$ to ultimately generate •OH is mechanistically significant:

$$O_2\bullet^- + O_2\bullet^- + 2H^+ \rightarrow H_2O_2 + O_2 \quad (3)$$

$$H_2O_2 + e^-CB \rightarrow \bullet OH + OH^- \quad (4)$$

The •OH observed in the photocatalytic systems containing $SrTiO_3$ could arise from two different routes, namely, the direct valence band oxidation of water/surface hydroxyls, and indirect $O_2\bullet^-$-mediated generation through Equations (3) and (4).

The valence-band holes created in $SrTiO_3$ represent some of the most oxidizing species that can be created in oxide semiconductor photocatalysis (+2.7–2.9 V vs. NHE) and have sufficient energy for the oxidation of water (E° = 1.23 V vs. NHE), organic molecules, and adsorbed hydroxyls [222]. The oxidation of surface OH^-/H_2O by h^+ is the main source of •OH formation:

$$h^+ + OH^-(\text{surface}) \rightarrow \bullet OH \quad (5)$$

$$h^+ + H_2O \rightarrow \bullet OH + H^+ \quad (6)$$

Efficiency of the above-mentioned reactions strongly depends on the degree of the surface coverage by OH^- radicals, which is controlled by the pH of the solution, crystallographic surface facets, and adsorbate presence. The higher pH leads to the increased density of OH^- radicals on the surface, promoting reaction (5) and, consequently, more effective •OH formation. On the contrary, in acidic conditions, water molecules will be the main h^+ acceptors through reaction (6). It is worth noting that in this case, the efficiency of •OH formation is lower due to the kinetic difficulty of water oxidation. Despite the numerous studies concerning •OH formation and its dependence on the pH for TiO_2, such investigations on $SrTiO_3$ are less common. However, the unique features of point of zero charge in $SrTiO_3$ create a unique surface chemistry in contrast to anatase TiO_2. Beyond •OH generation, valence band holes in $SrTiO_3$ can directly oxidize adsorbed organic molecules via a charge-transfer mechanism without hydroxyl radical mediation:

$$h^+ + R(\text{organic}) \rightarrow R\bullet^+ + (\text{subsequent degradation}) \quad (7)$$

The competition between •OH-mediated and direct h^+ oxidation reactions is determined by the type of substrate and may be studied through the use of fluorescence probes (either terephthalic acid or coumarin) along with the use of hole scavengers (methanol or EDTA). Specifically, the use of terephthalic acid does not take into account its dependence on pH conditions (2-hydroxyterephthalic acid is the fluorescent probe produced in this case). Similarly, experiments performed with coumarin are not always carried out at non-influential concentrations for the photocatalytic system [226]. A standardized, well-controlled approach to ROS quantification as supported by Nosaka et al. remains the exception rather than the rule in $SrTiO_3$ photocatalysis reports [227].

Theoretical computations using density functional theory (DFT) have offered important atomic-level information regarding the electronic structure of $SrTiO_3$ and associated ROS production. The utilization of hybrid density functionals has been successful in obtaining the experimentally reported band gap of $SrTiO_3$ (3.2–3.4 eV) with enhanced accuracy, and thus, their application for band edge computations has become the basic requirement for the accurate prediction of material properties [228]. Oxygen vacancy (V^o) is acknowledged as one of the most influential species in $SrTiO_3$ involved in ROS formation. Firstly, the oxygen defects create local donor states in the band gap of $SrTiO_3$ which promote light absorption. Secondly, the presence of such active sites on $SrTiO_3$ surfaces is conducive to the adsorption and activation of the O_2 molecule. The DFT calculations of O_2 adsorption energies on the surfaces of V^o-containing $SrTiO_3$ have shed light on the process of O_2 activation at defects. A theoretical study on h^+-promoted •OH production on the $SrTiO_3$ surface demands the need for precise calculations of the interaction between the photocatalyst and water molecules at the surface. It was found from ab initio molecular dynamics (AIMD) simulations of the interface between $SrTiO_3$ and water that there exists intricate hydrogen bonding in the interface that significantly affects the hydroxyl group surface density and its reactivity towards the h^+ ions [229]. Calculations show that the dissociation of water molecules at the $SrTiO_3$ surface is energetically favorable ($\Delta G < 0$). The theoretical framework for h^+-driven •OH formation has been further advanced by charge transfer calculations employing the constrained random phase approximation (cRPA) and time-dependent DFT (TD-DFT) approaches [230]. These techniques could in theory allow one to calculate the kinetics of hole transfer from the valence band of $SrTiO_3$ to surface OH^- groups. Most computational DFT studies of $SrTiO_3$ have focused solely on determining static adsorption energies and not kinetics of hole transfer. Thus, there exists an opportunity for future theoretical research in the area.

Utilization of $SrTiO_3$ in heterojunction systems with different semiconductor materials like *g*-C_3N_4, TiO_2, ZnO, and bismuth compounds is an important approach towards improving the efficiency of ROS production through enhanced spatial charge separation [231]. DFT modeling is one important tool that has helped predict the band alignment across these heterojunctions and the nature of charge transfer processes [232]. $\Delta\Phi$ is calculated using DFT predictions of electrostatic potential, which decides on either a staggered type-II or Z-scheme charge transfer process, and therefore its implication on ROS production. For type-II heterojunctions, electrons build up in the semiconductor with the lower conduction band edge, while holes accumulate in the semiconductor with the higher valence band edge. Although this design creates spatial separation between charge carriers, it limits the redox potentials of the system, it becomes impossible for accumulated electrons to reach low potentials to reduce oxygen to O_2^-, while holes will fail to reach sufficiently high potentials to oxidize water to •OH radicals. This thermodynamic consequence associated with charge separation in type-II heterojunctions is often disregarded, which emphasizes charge separation as an underlying reason for the increased efficiency of catalysis regardless of whether the redox potentials in the system are sufficient to generate ROS. Density functional theory

calculations of energy band offsets can serve as an effective tool for validation in this regard. Heterojunctions of Z-schemes that ensure the retention of the highest possible redox potentials for both semiconductor materials as well as spatial separation of charges have been widely studied as promising configurations involving $SrTiO_3$-based compounds [205]. In the case of $SrTiO_3$/*g*-C_3N_4 heterojunctions, the results of DFT calculations have shown that the electrostatic potential difference created at the interface between $SrTiO_3$ and *g*-C_3N_4 leads to charge transfer from $SrTiO_3$ to *g*-C_3N_4 (recombination) and from *g*-C_3N_4 to $SrTiO_3$ (recombination), leaving *g*-C_3N_4 electrons for O_2 reduction and $SrTiO_3$ holes for water oxidation intact [208].

7. Interfering Factors of Experimental Variables on the Photocatalytic Performance of $SrTiO_3$

The apparent rate constants cited for the $SrTiO_3$ photocatalysts differ from each other even in cases of similar modifications. The reason for such variations is not contradiction in photocatalytic chemistry but rather lies in the interaction of different parameters that affect the experiments independently within three categories: precursor chemistry, synthesis procedure and testing procedure. In the synthesis part, the most significant parameters influencing the activity are the precursor molar ratio Sr/Ti, mineraliser type, pH of synthesis solution, calcination temperature, and calcination atmosphere. All these factors individually vary in measured activity through change in phase composition, specific surface area, oxygen vacancy concentration, and dopants distribution. In the test procedure category, the spectrum of irradiation and its irradiance, model pollutant type, pH of the solution, ratio of the amount of catalyst to the optical saturation threshold and dark adsorption equilibration time can vary the result. Taking into account all sources of variability, the difference in the activities of SrTiO becomes understandable without contradicting the mechanism of photocatalysis itself.

The selection of titanium precursor plays an important role for the reactivity, crystal phase formation, and surface hydroxyl content of $SrTiO_3$. The alkoxide precursor, $Ti(OBu)_4$, readily hydrolyses under alkaline hydrothermal conditions, giving rise to the amorphous phase which crystallizes into anatase prior to its incorporation in the perovskite structure. Chloride precursor ($TiCl_4$) provides Cl^- ion as the competing ligand, which may deactivate the surface Ti atoms resulting in the reduction in surface hydroxyl content compared with $TiO_2 \cdot xH_2O$ precursors. The Sr/Ti molar ratio is one of the most influential synthesis parameters. In cases where Sr/Ti < 1.0, Ti-rich phase (TiO_2 and $SrTi_3O_7$) develops and acts independently in photocatalysis; hence, amplify the efficiency of $SrTiO_3$. Where Sr/Ti > 1.05, excess Sr forms $SrCO_3$ and $Sr(OH)_2$, passivating the surface sites of the photocatalyst.

The pH during the hydrothermal synthesis plays a major role in determining the speciation of the precursors, the surface charge on growing nuclei, and the mineralization potential of OH^- ions. At a pH below 10, the hydrolysis of Ti^{4+} species is not complete, and there will be formation of a mixture of amorphous and crystalline phases with low crystallinity and high defect concentration. The maximum crystallization force is obtained at a pH of 13–14, resulting in pure $SrTiO_3$ formation. However, different mineralizing agents like KOH or NaOH result in the addition of different cations, which act as A site dopants, thus causing unintentional doping and modified the electronic structure. Post-hydrothermal calcinations are commonly employed to enhance crystallinity and eliminate any remaining organic ligands from the alkoxide-derived materials. However, the calcination temperature has a significant influence on three interrelated parameters: (i) specific surface area: surface area falls exponentially at higher temperature due to sintering; (ii) concentration of oxygen vacancies, annealing in H_2/N_2 environment or

vacuum in the temperature range of 600–800 °C leads to formation of 10–50 times higher concentration of oxygen vacancies compared to air calcined samples; and (iii) distribution of dopants.

The light source might be the biggest source of variability in $SrTiO_3$ photocatalysis. The band gap energy of $SrTiO_3$ is around 3.2 eV, making this compound basically inactive when exposed to visible light. Studies using UV radiation in the region 250–380 nm show very active behavior of undoped $SrTiO_3$, whereas using a solar simulator, results show almost zero visible light activity of the exact same material. If the doped/heterostructure $SrTiO_3$ is tested in both cases, the difference in activity would be more than one order of magnitude. The organic dyes (methylene blue, rhodamine B, methyl orange) absorb visible light and can be directly photo-degraded via photosensitization in the presence of visible light independent of photocatalytic properties of the semiconductor. The process involves: dye molecule absorbs visible light photon, resulting in its excitation followed by transfer of an electron into the semiconductor conduction band and the generation of radicals which further oxidize the dye molecules. The contribution of this pathway may contribute 30–80% of the observed 'visible-light photocatalytic activity' in doped $SrTiO_3$ with MB or RhB as the probe. The rate of dye-sensitization depends on the surface area of the sample (determining the dye adsorption) rather than its band gap and thus higher surface areas result in more 'visible-light active' samples regardless of their true electronic nature.

8. Challenges and Limitations

Though there have been many significant developments in hydrothermally tuned $SrTiO_3$ towards photocatalytic water purification and water splitting, there are some scientific and technological barriers that hinder its industrial application.

The main problem associated with $SrTiO_3$ is its inherent large band gap (~3.2 eV). This results in light absorption predominantly in the ultraviolet (UV) range, which constitutes just a small portion of the total solar spectrum. While mid-gap states can be introduced or the bandgap narrowed by means of hydrothermal defect engineering and doping, too high a defect concentration may lead to recombination sites. Balancing increased absorption in the visible light and minimizing electron–hole recombination is a major challenge in designing this material. The exact control of the interfaces is complicated, particularly for hydrothermal synthesis of composite materials containing several different phases. Though an increased activity was reported in many works, thorough study of the charge transfer mechanisms and charge stability is usually missing.

In water purification using photocatalysis, the efficiency of the catalyst is tested using dye pollutants in controlled laboratory conditions. In reality, wastewater systems are complex, with matrices, competing ions, turbidity, and changing pH levels. These factors influence the effectiveness of the catalyst used. Another problem associated with catalysts used for water purification is their potential deactivation due to surface fouling, surface poisoning, or structural instability. While most catalysts show recyclability over three to five cycles, long-term stability is yet to be investigated. Overall water splitting without the use of sacrificial agents is still difficult for photocatalytic water splitting reactions. Another problem associated with hydrogen production is the use of noble metals as co-catalysts, which increases efficiency but increases the cost of the material and limits the scale-up process.

Another challenge is the economic viability of the hydrothermal method since the heating process is energy-consuming. Post-synthesis processes, such as calcination or reduction, require additional energy input, which makes the process economically unfeasible. Tackling such issues requires collaboration between the fields of materials chemistry, reactor

design, mechanistic spectroscopy, and techno-economics in order to move hydrothermal $SrTiO_3$ toward applications in water purification and hydrogen production.

9. Future Perspectives

Strategic materials design, understanding of mechanism, and engineering innovations represent the pathway towards future advancement of $SrTiO_3$ as a photocatalyst for wastewater treatment and water splitting processes.

One area of research includes the rational design of highly responsive $SrTiO_3$ systems that do not compromise charge carrier mobility. Defect engineering with particular attention to oxygen vacancies at optimal concentration levels is effective in improving visible light absorption but reducing recombination sites. Hydrothermal methods capable of achieving gradients in defect density or localized defects on surfaces might represent an exciting research opportunity in this area. Likewise, doping with elements showing synergetic effect in terms of band edge position could facilitate redox reactions. The use of two-dimensional materials or conductive carbon structures might help improve charge transport and absorption of visible light. Cocatalysts offer another area of potential development. The use of abundant transition metal phosphides, sulfides, carbides, or single-atom catalysts in place of expensive noble metals would drastically lower costs without compromising the ability of these materials to evolve hydrogen. Dual cocatalyst approaches specific to hydrogen and oxygen evolution reactions could lead to efficient water splitting without the need for sacrificial reagents.

Sustainable synthesis processes will be another focus of future work. Methods involving low-temperature hydrothermal treatments, microwave-assisted hydrothermal techniques, and solvent-free or biomass-derived precursor compounds will lower environmental impact. Process intensification and scaling will also be important considerations. Synergy between experiments and density functional theory (DFT) simulations along with machine learning algorithms would expedite the discovery process of optimal composition and morphology. Indeed, harnessing the potential of hydrothermal tuning of $SrTiO_3$ for hydrogen production and water purification using solar energy could be a promising approach toward sustainability. With adequate advances in materials science and engineering, scale-up, and systems integration, $SrTiO_3$ photocatalysis is poised to make an impact.

10. Conclusions

In conclusion, the utilization of $SrTiO_3$ as a photocatalyst within the family of perovskite oxides has emerged as a subject of considerable scientific interest and practical significance. A comprehensive survey of the literature reveals that $SrTiO_3$ possesses inherent photocatalytic activity owing to its characteristic perovskite structure and electronic properties.

One of its characteristics is the broad bandgap of about 3.2 eV, a hallmark feature of perovskite oxides like $SrTiO_3$. This property enables efficient absorption of solar radiation across a broad spectrum, rendering $SrTiO_3$ well-suited for solar-driven photocatalytic processes such as water oxidation, pollutant degradation, and organic synthesis. The surface morphology of $SrTiO_3$, a key aspect of perovskite oxides, plays a pivotal role in enhancing photocatalytic performance. Nano-structuring techniques, including nanoparticle synthesis and surface modification, have been employed to optimize surface area, promote charge transfer kinetics, and enhance light absorption efficiency, thereby amplifying the photocatalytic activity of $SrTiO_3$.

Additionally, the unique electronic structure of perovskite oxides like $SrTiO_3$ influences charge carrier dynamics and facilitates efficient charge separation, thus improving photocatalytic efficiency. Strategies such as heterojunction formation and dopant incorporation have been explored to tailor electronic properties and optimize charge transport

characteristics, thereby further enhancing photocatalytic performance. In practical applications, $SrTiO_3$-based photocatalysts exhibit potential across a spectrum of environmental and energy-related applications, such as water purification, air remediation, hydrogen production, and carbon dioxide reduction. The abundance, scalability, and environmental compatibility of perovskite oxides underscore $SrTiO_3$ as a promising candidate for sustainable photocatalysis.

Nevertheless, challenges such as photo corrosion susceptibility and charge carrier recombination remain areas of active investigation within the field of perovskite oxide photocatalysis. Addressing these challenges through advanced material design and synthesis methodologies will be crucial for realizing the full potential of $SrTiO_3$ and other perovskite oxides in photocatalytic applications.

In summary, $SrTiO_3$ demonstrates the promise of perovskite oxides as versatile and efficient photocatalysts, providing solutions to pressing environmental and energy challenges. Through continued research and innovation, perovskite oxide-based photocatalytic technologies hold the key to a sustainable and cleaner future.

Author Contributions: Conceptualization; methodology; validation; investigation; resources; data curation S.N., P.S. and A.S.R.; writing—original draft preparation S.N. and P.S.; writing—review and editing A.S.R. All authors have read and agreed to the published version of the manuscript.

Funding: This research received no external funding.

Data Availability Statement: Data is available on request.

Acknowledgments: Figure 2 has been modified using Google Gemini (3.5 Flash) by using our own generated image. Graphic Abstract has been generated and modified using Google Gemini (3.5 Flash).

Conflicts of Interest: The authors declare no conflicts of interest.

References

1. Huang, W.; Dai, J.; Xiong, L. Towards a sustainable energy future: Factors affecting solar-hydrogen energy production in China. *Sustain. Energy Technol. Assess.* **2022**, *52*, 102059. [CrossRef]
2. REN21 (2022) Renewables 2022—Global Status Report (Renewable Energies). 2022. Available online: https://www.ren21.net/gsr-2022 (accessed on 29 June 2026).
3. Royer, S.; Duprez, D.; Can, F.; Courtois, X.; Batiot-dupeyrat, C.; Laassiri, S.; Alamdari, H. Perovskites as substitutes of noble metals for heterogeneous catalysis: Dream or reality. *Chem. Rev.* **2014**, *114*, 10292–10368. [CrossRef] [PubMed]
4. Zhu, X.; Li, K.; Neal, L.M.; Li, F. Perovskites as geo-inspired oxygen storage materials for chemical looping and three-way catalysis—A perspective. *ACS Catal.* **2018**, *8*, 8213–8236. [CrossRef]
5. Kanhere, P.; Chen, Z. A review on visible light active perovskite-based photocatalysts. *Molecules* **2014**, *19*, 19995–20022. [CrossRef] [PubMed]
6. Shi, J.; Guo, L. ABO_3-based photocatalysts for water splitting. *Prog. Nat. Sci. Mater. Int.* **2012**, *22*, 592–615. [CrossRef]
7. Jiang, S.P.; Chan, S.H. A review of anode materials development in solid oxide fuel cells. *J. Mater. Sci.* **2004**, *39*, 4405–4439. [CrossRef]
8. Wang, C.H.; Chen, C.L.; Weng, H.S. Surface properties and catalytic performance of $La_{1-x}Sr_xFeO_3$ perovskite-type oxides for methane combustion. *Chemosphere* **2004**, *57*, 1131–1138. [CrossRef] [PubMed]
9. Cimino, S.; Lisi, L.; De Rossi, S.; Faticanti, M.; Porta, P. Methane combustion and CO oxidation on $LaAl_{1-x}Mn_xO_3$ perovskite-type oxide solid solutions. *Appl. Catal. B Environ.* **2003**, *43*, 397–406. [CrossRef]
10. Ciambelli, P.; Cimino, S.; Lasorella, G.; Lisi, L.; De Rossi, S.; Faticanti, M.; Minelli, G.; Porta, P. CO oxidation and methane combustion on $LaAl_{1-x}Fe_xO_3$ perovskite solid solutions. *Appl. Catal. B Environ.* **2002**, *37*, 231–241. [CrossRef]
11. Aliotta, C.; Liotta, L.F.F.; Deganello, F.; La Parola, V.; Martorana, A. Direct methane oxidation on $La_{1-x}Sr_xCr_{1-\gamma}Fe_\gamma O_3-\delta$ perovskite-type oxides as potential anode for intermediate temperature solid oxide fuel cells. *Appl. Catal. B Environ.* **2016**, *180*, 424–433. [CrossRef]
12. Huang, X.; Zhao, G.; Wang, G.; Irvine, J.T.S.S. Synthesis and applications of nanoporous perovskite metal oxides. *Chem. Sci.* **2018**, *9*, 3623–3637. [CrossRef] [PubMed]

13. Wang, Z.; Hong, J.; Ng, S.-F.; Liu, W.; Huang, J.; Chen, P.; Ong, W.-J. Recent progress of perovskite oxide in emerging photocatalysis landscape: Water splitting, CO_2 reduction, and N_2 fixation. *Acta Phys.-Chim. Sin.* **2021**, *37*, 2011033.
14. Mao, M.; Lv, H.; Li, Y.; Yang, Y.; Zeng, M.; Li, N.; Zhao, X. Metal Support Interaction in Pt Nanoparticles Partially Confined in the Mesopores of Microsized Mesoporous CeO_2 for Highly Efficient Purification of Volatile Organic Compounds. *ACS Catal.* **2016**, *6*, 418–427. [CrossRef]
15. Satoh, N.; Nakashima, T.; Kamikura, K.; Yamamoto, K. Quantum size effect in TiO_2 nanoparticles prepared by finely controlled metal assembly on dendrimer templates. *Nat. Nanotechnol.* **2008**, *3*, 106–111. [CrossRef] [PubMed]
16. Zhang, J.; Bang, J.H.; Tang, C.; Kamat, P.V. Tailored TiO_2-$SrTiO_3$ heterostructure nanotube arrays for improved photoelectrochemical performance. *ACS Nano* **2010**, *4*, 387–395. [CrossRef] [PubMed]
17. Biesuz, M.; Sglavo, V.M. Flash sintering of ceramics. *J. Eur. Ceram. Soc.* **2019**, *39*, 115–143. [CrossRef]
18. Royer, S.; Duprez, D. Catalytic Oxidation of Carbon Monoxide over Transition Metal Oxides. *ChemCatChem* **2011**, *3*, 24–65. [CrossRef]
19. Grabowska, E. Selected perovskite oxides: Characterization, preparation and photocatalytic properties—A review. *Appl. Catal. B Environ.* **2016**, *186*, 97–126. [CrossRef]
20. Zhu, H.; Zhang, P.; Dai, S. Recent Advances of Lanthanum-Based Perovskite Oxides for Catalysis. *ACS Catal.* **2015**, *5*, 6370–6385. [CrossRef]
21. de Oliveira, A.L.M.; Chantelle, L.; Figueiredo, J.F.D.; de Sousa Filho, I.A.; Lebullenger, R.; Deputier, S.; Weber, I.T.; Guilloux-Viry, M.; Santos, I.M.G.; Bouquet, V. $SrTi_{1-x}Sn_xO_3$ thin films as photocatalysts for organic dye degradation: Influence of the composition, deposition method, and growth orientation. In *Research Topics in Bioactivity, Environment and Energy*; Springer International Publishing: Berlin/Heidelberg, Germany, 2022; pp. 87–109.
22. Liu, Y.; Xie, L.; Li, Y.; Yang, R.; Qu, J.; Li, Y.; Li, X. Synthesis and high photocatalytic hydrogen production of $SrTiO_3$ nanoparticles from water splitting under UV irradiation. *J. Power Sources* **2008**, *183*, 701–707.
23. Nakashima, K.; Kera, M.; Fujii, I.; Wada, S. A new approach for the preparation of $SrTiO_3$ nanocubes. *Ceram. Int.* **2013**, *39*, 3231–3234.
24. Berbenni, V.; Marini, A.; Bruni, G. Effect of mechanical activation on the preparation of $SrTiO_3$ and Sr_2TiO_4 ceramics from the solid-state system $SrCO_3$–TiO_2. *J. Alloys Compd.* **2001**, *329*, 230–238.
25. Wang, T.X.; Liu, S.Z.; Chen, J. Molten salt synthesis of $SrTiO_3$ nanocrystals using nanocrystalline TiO_2 as a precursor. *Powder Technol.* **2011**, *205*, 289–291.
26. Zhang, J.; Huang, M.; Yanagisawa, K.; Yao, S. NaCl–H_2O-assisted preparation of $SrTiO_3$ nanoparticles by solid-state reaction at low temperature. *Ceram. Int.* **2015**, *41*, 5439–5444.
27. Yu, J.C.; Zhang, L.; Li, Q.; Kwong, K.W.; Xu, A.W.; Lin, J. Sonochemical preparation of nanoporous composites of titanium oxide and size-tunable strontium titanate crystals. *Langmuir* **2003**, *19*, 7673–7675. [CrossRef]
28. Bao, D.; Yao, X.; Wakiya, N.; Shinozaki, K.; Mizutani, N. Band-gap energies of sol-gel-derived $SrTiO_3$ thin films. *Appl. Phys. Lett.* **2001**, *79*, 3767–3769.
29. Levy, M.R. Chapter 3: Perovskite Perfect Lattice. In *Crystal Structure, Defect Properties and Prediction of Ceramic Materials*; University of London: London, UK, 2005; pp. 79–114.
30. Goldschmidt, V.M. Die Gesetze der Krystallochemie. *Naturwissenschaften* **1926**, *14*, 477–485. [CrossRef]
31. Zhang, C.; Ding, S.; Liu, G.; He, D.; Chen, P.; Wu, W.-Q.; Wang, L. Metal-doping for perovskite optoelectronic applications. *Mater. Today* **2025**, *89*, 172–191. [CrossRef]
32. Long, T.; Song, D.; Zhou, Y.; Yu, X.; Wang, X.; Li, C.; Chen, H.; Li, G.; He, F. Modulating activity of lattice oxygen of ABO_3 perovskite oxides in redox reactions: A review. *ACS Appl. Mater. Interfaces* **2025**, *17*, 20590–20612. [CrossRef] [PubMed]
33. Madelung, O.; Rössler, U.; Schulz, M. (Eds.) $SrTiO_3$: Crystal structure, physical properties. In *Landolt-Börnstein*; New Series, Group III, Volume 36A1; Springer: Berlin, Germany, 2001.
34. Wood, N.D.; Teter, D.M.; Tse, J.S.; Jackson, R.A.; Cooke, D.J.; Gillie, L.J.; Parker, S.C.; Molinari, M. An atomistic modelling investigation of the defect chemistry of $SrTiO_3$ and its Ruddlesden–Popper phases, $Sr_{n+1}Ti_nO_{3n+1}$ (n = 1–3). *J. Solid State Chem.* **2021**, *303*, 122523.
35. Bartel, C.J.; Sutton, C.; Goldsmith, B.R.; Ouyang, R.; Musgrave, C.B.; Ghiringhelli, L.M.; Scheffler, M. New tolerance factor to predict the stability of perovskite oxides and halides. *Sci. Adv.* **2019**, *5*, eaav0693. [CrossRef] [PubMed]
36. Marques, C. Advanced Si Pad Detector Development and $SrTiO_3$ Studies by Emission Channeling and Hyperfine Interaction Experiments. Doctoral Dissertation, Universidade de Lisboa, Lisbon, Portugal, 2009.
37. Hayward, S.A.; Salje, E.K.H. Cubic-tetragonal phase transition in $SrTiO_3$ revisited: Landau theory and transition mechanism. *Phase Transit.* **1999**, *68*, 501–522. [CrossRef]
38. Lytle, F.W. X-ray diffractometry of low-temperature phase transformations in strontium titanate. *J. Appl. Phys.* **1964**, *35*, 2212–2215. [CrossRef]
39. Revie, P. Dielectric Properties of $SrTiO_3$ at Low Temperature. *Phys. Rev. Lett.* **1971**, *26*, 851–853.

40. Saraf, S.; Riess, I.; Rothschild, A. Parallel Band and Hopping Electron Transport in $SrTiO_3$. *Adv. Electron. Mater.* **2016**, *2*, 1500368. [CrossRef]
41. De Souza, R.A. Oxygen Diffusion in $SrTiO_3$ and Related Perovskite Oxides. *Adv. Funct. Mater.* **2015**, *25*, 6326–6342. [CrossRef]
42. Verbraeken, M.C.; Ramos, T.; Agersted, K.; Ma, Q.; Savaniu, C.D.; Sudireddy, B.R.; Irvine, J.T.S.; Holtappels, P.; Tietz, F. Modified strontium titanates: From defect chemistry to SOFC anodes. *RSC Adv.* **2015**, *5*, 1168–1180. [CrossRef]
43. Merkle, R.; Maier, J. How Is Oxygen Incorporated into Oxides? A Comprehensive Kinetic Study of a Simple Solid-State Reaction with $SrTiO_3$ as a Model Material. *Angew. Chem. Int. Ed.* **2008**, *47*, 3874–3894. [CrossRef] [PubMed]
44. Segal, D. Chemical synthesis of ceramic materials. *J. Mater. Chem.* **1997**, *7*, 1297–1305. [CrossRef]
45. Wang, N.; Kong, D.; He, H. Solvothermal synthesis of strontium titanate nanocrystallines from metatitanic acid and photocatalytic activities. *Powder Technol.* **2011**, *207*, 470–473. [CrossRef]
46. Athayde, D.D.; Souza, D.F.; Silva, A.M.A.; Vasconcelos, D.; Nunes, E.H.M.; Diniz da Costa, J.C.; Vasconcelos, W.L. Review of perovskite ceramic synthesis and membrane preparation methods. *Ceram. Int.* **2015**, *42*, 6555–6571. [CrossRef]
47. Konta, R.; Kato, H.; Kobayashi, H.; Kudo, A. Photophysical properties and photocatalytic activities under visible light irradiation of silver vanadates. *Phys. Chem. Chem. Phys.* **2003**, *5*, 3061–3065. [CrossRef]
48. Dhanasekaran, P.; Gupta, N.M. Factors affecting the production of H_2 by water splitting over a novel visible-light-driven photocatalyst $GaFeO_3$. *Int. J. Hydrogen Energy* **2012**, *37*, 4897–4907. [CrossRef]
49. Baharuddin, N.A.; Muchtar, A.; Somalu, M.R. Preparation of $SrFe_{0.5}Ti_{0.5}O_3-\delta$ perovskite-structured ceramic using the glycine-nitrate combustion technique. *Mater. Lett.* **2017**, *194*, 197–201. [CrossRef]
50. Modeshia, D.R.; Darton, R.J.; Ashbrook, S.E.; Walton, R.I. Control of polymorphism in $NaNbO_3$ by hydrothermal synthesis. *Chem. Commun.* **2009**, *1*, 68–70.
51. Mann, M.; Jackson, S.; Kolis, J. Hydrothermal crystal growth of the potassium niobate and potassium tantalate family of crystals. *J. Solid State Chem.* **2010**, *183*, 2675–2680. [CrossRef]
52. Yun, B.K.; Koo, Y.S.; Jung, J.H.; Song, M.; Yoon, S. Possible role of hydroxyl group on local structure and phase transition of $KNbO_3$ and $KTaO_3$ nanocrystals. *Phys. B Condens. Matter.* **2010**, *405*, 4866–4870. [CrossRef]
53. Rabenau, A. The Role of Hydrothermal Synthesis in Preparative Chemistry. *Angew. Chem. Int. Ed. Engl.* **1985**, *24*, 1026–1040. [CrossRef]
54. Yang, Q.; Lu, Z.; Liu, J.; Lei, X.; Chang, Z.; Luo, L.; Sun, X. Metal oxide and hydroxide nanoarrays: Hydrothermal synthesis and applications as supercapacitors and nanocatalysts. *Prog. Nat. Sci. Mater. Int.* **2013**, *23*, 351–366. [CrossRef]
55. Schiopu, A.-G.; Iordache, D.M.; Oproescu, M.; Cursaru, L.M.; Ioța, A.-M. Tailoring the synthesis method of metal oxide nanoparticles for desired properties. *Crystals* **2024**, *14*, 899. [CrossRef]
56. Anaya-Zavaleta, J.C.; Ledezma-Pérez, A.S.; Gallardo-Vega, C.; Rodríguez-Hernández, J.; Alvarado-Canché, C.N.; García-Casillas, P.E.; de León, A.; Herrera-May, A.L. ZnO nanoparticles by hydrothermal method: Synthesis and characterization. *Technologies* **2025**, *13*, 18. [CrossRef]
57. Belew, A.A.; Assege, M.A. Solvothermal synthesis of metal oxide nanoparticles: A review of applications, challenges, and future perspectives. *Results Chem.* **2025**, *16*, 102438. [CrossRef]
58. Tazim, T.Q.; Kawsar, M.; Hossain, M.S.; Bahadur, N.M.; Ahmed, S. Hydrothermal synthesis of nano-metal oxides for structural modification: A review. *Next Nanotechnol.* **2025**, *7*, 100167. [CrossRef]
59. Nandagudi, A.; Nagarajarao, S.H.; Santosh, M.S.; Basavaraja, B.M.; Malode, S.J.; Mascarenhas, R.J.; Shetti, N.P. Hydrothermal synthesis of transition metal oxides, transition metal oxide/carbonaceous material nanocomposites for supercapacitor applications. *Mater. Today Sustain.* **2022**, *19*, 100214. [CrossRef]
60. Flaschen, S.S. An aqueous synthesis of barium titanate. *J. Am. Chem. Soc.* **1955**, *77*, 6194. [CrossRef]
61. Kumada, N.; Dong, Q.; Yonesaki, Y.; Takei, T.; Kinomura, N. Hydrothermal synthesis of $NaNbO_3$—Morphology change by starting compounds. *J. Ceram. Soc. Jpn.* **2011**, *119*, 483–485. [CrossRef]
62. Rachakom, A.; Jiansirisomboon, S.; Watcharapasorn, A. Effect of poling on piezoelectric and ferroelectric properties of $Bi_{0.5}Na_{0.5}Ti_{1-x}Zr_xO_3$ ceramics. *J. Electroceram.* **2014**, *33*, 105–110. [CrossRef]
63. Shi, G.; Wang, J.; Wang, H.; Wu, Z.; Wu, H. Hydrothermal synthesis of morphology-controlled $KNbO_3$, $NaNbO_3$, and (K, Na)NbO_3 powders. *Ceram. Int.* **2017**, *43*, 7222–7230. [CrossRef]
64. Nakashima, K.; Toshima, Y.; Kobayashi, Y.; Ishikawa, Y.; Kakihana, M. Solvothermal synthesis and morphology control of $NaNbO_3$ nanocubes using a reaction medium of water and/or methanol. *J. Asian Ceram. Soc.* **2019**, *7*, 544–550.
65. López-Juárez, R.; Castañeda-Guzmán, R.; Villafuerte-Castrejón, M.E. Fast synthesis of $NaNbO_3$ and $K_{0.5}Na_{0.5}NbO_3$ by microwave hydrothermal method. *Ceram. Int.* **2014**, *40*, 14757–14764.
66. Oliveira, M.C.; Gracia, L.; de Assis, M.; Rosa, I.L.; do Carmo Gurgel, M.F.; Longo, E.; Andres, J. Mechanism of photoluminescence in intrinsically disordered $CaZrO_3$ crystals: First principles modeling of the excited electronic states. *J. Alloys Compd.* **2017**, *722*, 981–995.

67. Boschini, F.; Rulmont, A.; Cloots, R.; Vertruyen, B. Rapid synthesis of submicron crystalline barium zirconate $BaZrO_3$ by precipitation in aqueous basic solution below 100 °C. *J. Eur. Ceram. Soc.* **2009**, *29*, 1457–1462.
68. Yamaguchi, Y.; Fukushima, M.; Ito, S.; Fujimoto, K. Low-temperature solid-state synthesis of perovskite oxides under 50 °C. *Chem. Lett.* **2016**, *45*, 226–228. [CrossRef]
69. Dong, Z.; Ye, T.; Zhao, Y.; Yu, J.; Wang, F.; Zhang, L.; Wang, X.; Guo, S. Perovskite $BaZrO_3$ hollow micro- and nanospheres: Controllable fabrication, photoluminescence and adsorption of reactive dyes. *J. Mater. Chem.* **2011**, *21*, 5978–5984. [CrossRef]
70. Kanie, K.; Seino, Y.; Matsubara, M.; Muramatsu, A. Size-controlled hydrothermal synthesis of monodispersed $BaZrO_3$ sphere particles by seeding. *Adv. Powder Technol.* **2017**, *28*, 55–60. [CrossRef]
71. Kanie, K.; Seino, Y.; Matsubara, M.; Nakaya, M.; Muramatsu, A. Hydrothermal synthesis of $BaZrO_3$ fine particles controlled in size and shape and fluorescence behavior by europium doping. *New J. Chem.* **2014**, *38*, 3548–3555.
72. Zhang, H.; Qiao, J.; Li, G.; Li, S.; Wang, G.; Wang, J.; Song, Y. Preparation of Ce^{4+}-doped $BaZrO_3$ by hydrothermal method and application in dual-frequent sonocatalytic degradation of norfloxacin in aqueous solution. *Ultrason. Sonochem.* **2018**, *42*, 356–367. [CrossRef] [PubMed]
73. Spooren, J.; Walton, R.I. Hydrothermal synthesis of the perovskite manganites $Pr_{0.5}Sr_{0.5}MnO_3$ and $Nd_{0.5}Sr_{0.5}MnO_3$ and alkali-earth manganese oxides $CaMn_2O_4$, 4H-$SrMnO_3$, and 2H-$BaMnO_3$. *J. Solid State Chem.* **2005**, *178*, 1683–1691. [CrossRef]
74. Weber, M.C.; Kreisel, J.; Thomas, P.A.; Newton, M.; Sardar, K.; Walton, R.I. Phonon Raman scattering of $RCrO_3$ perovskites (R = Y, La, Pr, Sm, Gd, Dy, Ho, Yb, Lu). *Phys. Rev. B* **2012**, *85*, 054303.
75. Daniels, L.M.; Weber, M.C.; Lees, M.R.; Guennou, M.; Kashtiban, R.J.; Sloan, J.; Kreisel, J.; Walton, R.I. Structures and magnetism of the rare-earth orthochromite perovskite solid solution $La_xSm_{1-x}CrO_3$. *Inorg. Chem.* **2013**, *52*, 12161–12169. [PubMed]
76. Wang, S.; Huang, K.; Zheng, B.; Zhang, J.; Feng, S. Mild hydrothermal synthesis and physical property of perovskite Sr doped $LaCrO_3$. *Mater. Lett.* **2013**, *101*, 86–89. [CrossRef]
77. Hou, C.; Feng, W.; Yuan, L.; Huang, K.; Feng, S. Crystal facet control of $LaFeO_3$, $LaCrO_3$, and $La_{0.75}Sr_{0.25}MnO_3$. *CrystEngComm* **2014**, *16*, 2874–2877. [CrossRef]
78. Yuan, L.; Huang, K.; Wang, S.; Hou, C.; Wu, X.; Zou, B.; Feng, S. Crystal shape tailoring in perovskite structure rare-earth ferrites $REFeO_3$ (RE = La, Pr, Sm, Dy, Er, and Y) and shape-dependent magnetic properties of $YFeO_3$. *Cryst. Growth Des.* **2016**, *16*, 6522–6530. [CrossRef]
79. Huang, K.; Yuan, L.; Feng, S. Crystal facet tailoring arts in perovskite oxides. *Inorg. Chem. Front.* **2015**, *2*, 965–981. [CrossRef]
80. Kim, H.; Alshareef, H.N. MXetronics: MXene-enabled electronic and photonic devices. *ACS Mater. Lett.* **2019**, *2*, 55–70. [CrossRef]
81. Shi, H.; Li, X.; Wang, D.; Yuan, Y.; Zou, Z.; Ye, J. $NaNbO_3$ nanostructures: Facile synthesis, characterization, and their photocatalytic properties. *Catal. Lett.* **2009**, *132*, 205–212. [CrossRef]
82. Gu, Q.; Zhu, K.; Zhang, N.; Sun, Q.; Liu, P.; Liu, J.; Wang, J.; Li, Z. Modified solvothermal strategy for straightforward synthesis of cubic $NaNbO_3$ nanowires with enhanced photocatalytic H_2 evolution. *J. Phys. Chem. C* **2015**, *119*, 25956–25964.
83. Ban, T.; Kaiden, T.; Ohya, Y. Hydrothermal synthesis of layered perovskite-structured metal oxides and cesium tungstate nanosheets. *Cryst. Growth Des.* **2019**, *19*, 6903–6910. [CrossRef]
84. Querejeta, A.; Varela, A.; Parras, M.; Monte, F.D.; García-Hernández, M.; González-Calbet, J.M. Hydrothermal synthesis: A suitable route to elaborate nanomanganites. *Chem. Mater.* **2009**, *21*, 1898–1905. [CrossRef]
85. Yao, L.; Pan, Z.; Zhai, J.; Chen, H.H. Novel design of highly [110]-oriented barium titanate nanorod array and its application in nanocomposite capacitors. *Nanoscale* **2017**, *9*, 4255–4264. [CrossRef] [PubMed]
86. Eckert, M. Max von Laue and the discovery of X-ray diffraction in 1912. *Ann. Phys.* **2012**, *524*, 83–85. [CrossRef]
87. Bragg, W.H.; Bragg, W.L. The structure of some crystals as indicated by their diffraction of X-rays. *Proc. R. Soc. Lond. A* **1913**, *89*, 248–277. [CrossRef]
88. Hull, A.W. A New Method of Chemical Analysis. *J. Am. Chem. Soc.* **1919**, *41*, 1168–1175. [CrossRef]
89. Walton, R.I. Perovskite oxides prepared by hydrothermal and solvothermal synthesis: A review of crystallisation, chemistry, and compositions. *Chem. Eur. J.* **2020**, *26*, 9041–9069. [CrossRef] [PubMed]
90. Mourão, H.A.; Lopes, O.F.; Ribeiro, C.; Mastelaro, V.R. Rapid hydrothermal synthesis and pH-dependent photocatalysis of strontium titanate microspheres. *J. Mater. Sci. Mater. Electron. Process.* **2015**, *30*, 651–657. [CrossRef]
91. Moreira, M.L.; Mambrini, G.P.; Volanti, D.P.; Leite, E.R.; Orlandi, M.O.; Pizani, P.S.; Varela, J.A. Hydrothermal microwave: A new route to obtain photoluminescent crystalline $BaTiO_3$ nanoparticles. *Chem. Mater.* **2008**, *20*, 5381–5387. [CrossRef]
92. Souza, A.E.; Santos, G.T.A.; Barra, B.C.; Macedo, W.D., Jr.; Teixeira, S.R.; Santos, C.M.; Longo, E. Photoluminescence of $SrTiO_3$: Influence of particle size and morphology. *Cryst. Growth Des.* **2012**, *12*, 5671–5679. [CrossRef]
93. Zhang, Y.; Zhong, L.; Duan, D. Single-step hydrothermal synthesis of strontium titanate nanoparticles from crystalline anatase titanium dioxide. *Ceram. Int.* **2015**, *41*, 13516–13524. [CrossRef]
94. Lin, H.-Y.; Cian, L.-T. Microwave-assisted hydrothermal synthesis of $SrTiO_3$:Rh for photocatalytic Z-scheme overall water splitting. *Appl. Sci.* **2019**, *9*, 55.

95. Crosby, L.A.; Chen, B.R.; Kennedy, R.M. All roads lead to TiO_2: TiO_2-rich surfaces of barium and strontium titanate prepared by hydrothermal synthesis. *Chem. Mater.* **2018**, *30*, 841–846.
96. Phoon, B.L.; Lai, C.W.; Pan, G.T.; Yang, T.C.K.; Juan, J.C. One-pot hydrothermal synthesis of strontium titanate nanoparticles photoelectrode using electrophoretic deposition for enhancing photoelectrochemical water splitting. *Ceram. Int.* **2018**, *44*, 9923–9933. [CrossRef]
97. Kiss, B.; Manning, T.D.; Hesp, D.; Didier, C.; Taylor, A.; Pickup, D.M.; Chadwick, A.V.; Allison, H.E.; Dhanak, V.R.; Claridge, J.B.; et al. Nano-structured rhodium doped $SrTiO_3$–Visible light activated photocatalyst for water decontamination. *Appl. Catal. B Environ.* **2017**, *206*, 547–555.
98. Wu, G.; Li, P.; Xu, D.; Luo, B.; Hong, Y.; Shi, W.; Liu, C. Hydrothermal synthesis and visible-light-driven photocatalytic degradation of tetracycline by Mn-doped $SrTiO_3$ nanocubes. *Appl. Surf. Sci.* **2015**, *333*, 39–47.
99. Huang, S.-T.; Lee, W.W.; Chang, J.L.; Huang, W.S.; Chou, S.Y.; Chen, C.C. Hydrothermal synthesis of $SrTiO_3$ nanocubes: Characterization, photocatalytic activities, and degradation pathway. *J. Taiwan Inst. Chem. Eng.* **2014**, *45*, 1927–1936.
100. Putri, Y.E.; Wendari, T.P.; Dinda, D.; Arnel, M.; Faradilla, H.; Refinel, R.; Efdi, M. The hydrothermal synthesis of $SrTiO_3$ nanopolyhedral with the assistance of surfactants and their optical characteristics. *Case Stud. Chem. Environ. Eng.* **2024**, *9*, 100601.
101. Thesing, A.; Loguercio, L.F.; Silva, E.A.; Franciosi, G.; Véliz, A.B.L.; Khattak, M.R.K.; Brolo, A.G.; Santos, M.J.L.; Santos, J.F.L. Engineering $SrTiO_3$ nanostructures for enhanced photocatalytic performance: Unveiling the influence of titanium precursors and synthesis temperature. *ACS Omega* **2025**, *10*, 40066–40075. [CrossRef] [PubMed]
102. Shen, H.; Lu, Y.; Wang, Y.; Pan, Z.; Cao, G.; Yan, X.; Fang, G. Low-temperature hydrothermal synthesis of $SrTiO_3$ nanoparticles without alkali and their effective photocatalytic activity. *J. Adv. Ceram.* **2016**, *5*, 298–307.
103. Yang, D.; Zhao, X.; Zou, X.; Zhou, Z.; Jiang, Z. Removing Cr(VI) in water via visible-light photocatalytic reduction over Cr-doped $SrTiO_3$ nanoplates. *Chemosphere* **2019**, *215*, 586–595. [CrossRef] [PubMed]
104. Kato, K.; Jiang, J.; Sakata, Y.; Yamakata, A. Effect of Na-doping on electron decay kinetics in $SrTiO_3$ photocatalyst. *ChemCatChem* **2019**, *11*, 6349–6354.
105. Wang, Y.Q.; Lian, W.; Liu, Y. Electronic structure and optical properties in alkaline-earth metals (A = Mg, Ca, Ba) and Ir co-doped $SrTiO_3$: A DFT + U investigation. *Optik* **2021**, *228*, 166128. [CrossRef]
106. Nguyen, C.V.; Trang, T.N.Q.; Pham, H.Q.; Thu, V.T.H.; Ho, V.T.T. One-step heating hydrothermal of iridium-doped cubic perovskite strontium titanate towards hydrogen evolution. *Mater. Lett.* **2021**, *282*, 128686. [CrossRef]
107. Wang, J.; Yin, S.; Komatsu, M.; Zhang, Q.; Saito, F.; Sato, T. Preparation and characterization of nitrogen-doped $SrTiO_3$ photocatalyst. *J. Photochem. Photobiol. A Chem.* **2004**, *165*, 149–156.
108. Shan, J.; Raziq, F.; Humayun, M.; Zhou, W.; Qu, Y.; Wang, G.; Li, Y. Improved charge separation and surface activation via boron-doped layered polyhedron $SrTiO_3$ for co-catalyst-free photocatalytic CO_2 conversion. *Appl. Catal. B Environ.* **2017**, *219*, 10–17. [CrossRef]
109. Sun, D.; Zhang, Y.; Yan, S.; Sun, K.; Wang, G.; Bu, Y.; Xie, G. Fabrication of excellent heterojunction assisting by interfaced oxygen vacancy to improve the separation capacity of photogenerated carriers. *Adv. Mater. Interfaces* **2018**, *5*, 1701325. [CrossRef]
110. Opoku, F.; Govender, K.K.; van Sittert, C.G.C.E.; Govender, P.P. Hybrid DFT studies of MWCNT/Zr-doped $SrTiO_3$ heterostructure: Hydrogen production, electronic properties and charge carrier mediator role of Zr^{4+} ion. *Int. J. Hydrogen Energy* **2018**, *43*, 22253–22264. [CrossRef]
111. Hou, Y.S.; Wu, R.Q. Hybrid density functional study of band-gap engineering of $SrTiO_3$ photocatalyst via doping for water splitting. *J. Phys. Chem. C* **2021**, *125*, 14684–14693. [CrossRef]
112. Wang, J.; Wang, X.; Liu, G.; Cheng, H.M. Engineering perovskite photocatalysts through isovalent cation substitution for enhanced charge transport. *J. Mater. Chem. A* **2022**, *10*, 8124–8142. [CrossRef]
113. Hao, Y.; Li, J.; Wang, S.; Li, Y.; Zhang, Z. Oxygen-vacant semiconductor photocatalysts. *Adv. Funct. Mater.* **2021**, *31*, 2100919. [CrossRef]
114. Ma, H.; Yang, W.; Tang, H.; Pan, Y.; Li, W.; Fang, R.; Shen, Y.; Dong, F. Enhance the stability of oxygen vacancies in $SrTiO_3$ via metallic Ag modification for efficient and durable photocatalytic NO abatement. *J. Hazard. Mater.* **2023**, *452*, 131269. [CrossRef] [PubMed]
115. Kato, H.; Asakura, K.; Kudo, A. Highly efficient water splitting into H_2 and O_2 over lanthanum-doped $NaTaO_3$ photocatalysts. *J. Am. Chem. Soc.* **2003**, *125*, 3082–3089. [CrossRef] [PubMed]
116. Konta, R.; Ishii, T.; Kato, H.; Kudo, A. Photocatalytic activities of noble-metal-ion-doped $SrTiO_3$ under visible-light irradiation. *J. Phys. Chem. B* **2004**, *108*, 8992–8995. [CrossRef]
117. Zhan, F.; Wen, G.; Li, R.; Feng, C.; Liu, Y.; Zhu, M.; Zheng, Y.; Zhao, Y.; La, P. A comprehensive review of oxygen vacancy modified photocatalysts: Synthesis, characterization and applications. *Phys. Chem. Chem. Phys.* **2024**, *26*, 11182–11207. [CrossRef] [PubMed]
118. Kalra, P.; Ghosh, D.; Ingole, P.P. Favoring product desorption by a tailored electronic environment of oxygen vacancies in Cr doped $SrTiO_3$. *ACS Appl. Mater. Interfaces* **2023**, *15*, 30187–30198. [CrossRef] [PubMed]

119. Wang, Z.; Hisatomi, T.; Domen, K. Photocatalytic overall water splitting by $SrTiO_3$: Progress report and design strategies. *ACS Appl. Energy Mater.* **2023**, *6*, 1501–1525.
120. Hisatomi, T.; Kubota, J.; Domen, K. Recent advances in semiconductors for photocatalytic and photoelectrochemical water spliting. *Chem. Soc. Rev.* **2014**, *43*, 7520–7535. [PubMed]
121. Kabir, E.; Kumar, P.; Kumar, S.; Adelodun, A.A.; Kim, K.H. Solar energy: Potential and future prospects. *Renew. Sustain. Energy Rev.* **2018**, *82*, 894–900. [CrossRef]
122. Zeng, S.; Kar, P.; Thakur, U.K.; Shankar, K. A review on photocatalytic CO_2 reduction using perovskite oxide nanomaterials. *Nanotechnology* **2018**, *29*, 052001. [CrossRef] [PubMed]
123. Schlapbach, L.; Züttel, A. Hydrogen-storage materials for Mobile Applications. *Nature* **2002**, *414*, 353–358. [CrossRef] [PubMed]
124. Zollinger, H. *Color Chemistry: Synthesis, Properties, and Applications of Organic Dyes and Pigments*, 3rd ed.; John Wiley & Sons, Ltd.: Hoboken, NJ, USA, 2003. [CrossRef]
125. Houas, A.; Lachheb, H.; Ksibi, M.; Elaloui, E.; Guillard, C.; Herrmann, J.-M. Photocatalytic degradation pathway of methylene blue in water. *Appl. Catal. B Environ.* **2001**, *31*, 145–157. [CrossRef]
126. Al-Tohamy, R.; Ali, S.S.; Li, F.; Okasha, K.M.; Mahmoud, Y.A.-G.; Elsamahy, T.; Jiao, H.; Fu, Y.; Sun, J. A critical review on the treatment of dye-containing wastewater: Ecotoxicological and health concerns of textile dyes and possible remediation approaches for environmental safety. *Ecotoxicol. Environ. Saf.* **2022**, *231*, 113160. [CrossRef] [PubMed]
127. Larsson, D.G.J. Antibiotics in the environment. *Ups. J. Med. Sci.* **2014**, *119*, 108–112. [CrossRef] [PubMed]
128. Forgacs, E.; Cserháti, T.; Oros, G. Removal of synthetic dyes from wastewaters: A review. *Environ. Int.* **2004**, *30*, 953–971. [CrossRef] [PubMed]
129. Bhatkhande, D.S.; Pangarkar, V.G.; Beenackers, A.A.C.M. Photocatalytic degradation for environmental applications—A review. *J. Chem. Technol. Biotechnol.* **2002**, *77*, 102–116. [CrossRef]
130. Maeda, K. Photocatalytic water splitting using semiconductor particles: History and recent developments. *J. Photochem. Photobiol. C Photochem. Rev.* **2011**, *12*, 237–268. [CrossRef]
131. Wang, W.; Tadé, M.O.; Shao, Z. Research progress of perovskite materials in photocatalysis- and photovoltaics-related energy conversion and environmental treatment. *Chem. Soc. Rev.* **2015**, *44*, 5371–5408. [CrossRef] [PubMed]
132. Chong, M.N.; Jin, B.; Chow, C.W.K.; Saint, C. Recent developments in photocatalytic water treatment technology: A review. *Water Res.* **2010**, *44*, 2997–3027. [CrossRef] [PubMed]
133. Kudo, A.; Miseki, Y. Heterogeneous photocatalyst materials for water splitting. *Chem. Soc. Rev.* **2009**, *38*, 253–278. [CrossRef] [PubMed]
134. Jafari, T.; Moharreri, E.; Amin, A.S.; Miao, R.; Song, W.; Suib, S.L. Photocatalytic water splitting—The untamed dream: A review of recent advances. *Molecules* **2016**, *21*, 900. [CrossRef] [PubMed]
135. Ni, M.; Leung, M.K.H.; Leung, D.Y.C.; Sumathy, K. A review and recent developments in photocatalytic water-splitting using TiO_2 for hydrogen production. *Renew. Sustain. Energy Rev.* **2007**, *11*, 401–425. [CrossRef]
136. Maeda, K.; Murakami, N.; Ohno, T. Dependence of activity of rutile titanium(IV) oxide powder for photocatalytic overall water splitting on structural properties. *J. Phys. Chem. C* **2014**, *118*, 9093–9100. [CrossRef]
137. Melián, E.P.; Díaz, O.G.; Méndez, A.O.; López, C.R.; Suárez, M.N.; Rodríguez, J.M.D.; Navío, J.A.; Hevia, D.F.; Peña, J.P. Efficient and affordable hydrogen production by water photo-splitting using TiO_2-based photocatalysts. *Int. J. Hydrogen Energy* **2013**, *38*, 2144–2155. [CrossRef]
138. Ham, Y.; Hisatomi, T.; Goto, Y.; Moriya, Y.; Sakata, Y.; Yamakata, A.; Kubota, J.; Domen, K. Flux-mediated doping of $SrTiO_3$ photocatalysts for efficient overall water splitting. *J. Mater. Chem. A* **2016**, *4*, 3027–3033. [CrossRef]
139. Niishiro, R.; Tanaka, S.; Kudo, A. Hydrothermal-synthesized $SrTiO_3$ photocatalyst codoped with rhodium and antimony with visible-light response for sacrificial H_2 and O_2 evolution and application to overall water splitting. *Appl. Catal. B Environ.* **2014**, *150–151*, 187–196. [CrossRef]
140. Mu, L.; Zhao, Y.; Li, A.; Wang, S.; Wang, Z.; Yang, J.; Wang, Y.; Liu, T.; Chen, R.; Zhu, J.; et al. Enhancing charge separation on high symmetry $SrTiO_3$ exposed with anisotropic facets for photocatalytic water splitting. *Energy Environ. Sci.* **2016**, *9*, 2463–2469. [CrossRef]
141. Tüysüz, H.; Chan, C.K. Preparation of amorphous and nanocrystalline sodium tantalum oxide photocatalysts with porous matrix structure for overall water splitting. *Nano Energy* **2013**, *2*, 116–123. [CrossRef]
142. Modak, B.; Ghosh, S.K. Improvement of photocatalytic activity of $NaTaO_3$ under visible light by N and F doping. *Chem. Phys. Lett.* **2014**, *613*, 54–58. [CrossRef]
143. Wahab, A.K.; Odedairo, T.; Labis, J.; Hedhili, M.; Delavar, A.; Idriss, H. Comparing $Pt/SrTiO_3$ to $Rh/SrTiO_3$ for hydrogen photocatalytic production from ethanol. *Arab. J. Sci. Eng.* **2013**, *38*, 83–89. [CrossRef]
144. Domen, K.; Kudo, A.; Onishi, T.; Kosugi, N.; Kuroda, H. Photocatalytic decomposition of water into hydrogen and oxygen over nickel(II) oxide-strontium titanate ($SrTiO_3$) powder. 1. Structure of the catalysts. *J. Phys. Chem.* **1986**, *90*, 292–295. [CrossRef]

145. Alammar, T.; Hamm, I.; Wark, M.; Mudring, A.V. Low-temperature route to metal titanate perovskite nanoparticles for photocatalytic applications. *Appl. Catal. B Environ.* **2015**, *178*, 20–28. [CrossRef]
146. Wang, Q.; Hisatomi, T.; Jia, Q.; Tokudome, H.; Zhong, M.; Wang, C.; Pan, Z.; Takata, T.; Nakabayashi, M.; Shibata, N.; et al. Scalable water splitting on particulate photocatalyst sheets with a solar-to-hydrogen energy conversion efficiency exceeding 1%. *Nat. Mater.* **2016**, *15*, 611–615. [CrossRef] [PubMed]
147. Wang, Q.; Hisatomi, T.; Ma, S.S.K.; Li, Y.; Domen, K. Core/Shell Structured La- and Rh-Codoped $SrTiO_3$ as a Hydrogen Evolution Photocatalyst in Z-Scheme Overall Water Splitting under Visible Light Irradiation. *Chem. Mater.* **2014**, *26*, 4144–4150. [CrossRef]
148. Shen, P.; Lofaro, J.C.; Woerner, W.R.; White, M.G.; Su, D.; Orlov, A. Photocatalytic activity of hydrogen evolution over Rh doped $SrTiO_3$ prepared by polymerizable complex method. *Chem. Eng. J.* **2013**, *223*, 200–208. [CrossRef]
149. Zou, J.-P.P.; Zhang, L.-Z.Z.; Luo, S.-L.L.; Leng, L.-H.H.; Luo, X.-B.B.; Zhang, M.-J.J.; Luo, Y.; Guo, G.-C.C. Preparation and photocatalytic activities of two new Zn-doped $SrTiO_3$ and $BaTiO_3$ photocatalysts for hydrogen production from water without cocatalysts loading. *Int. J. Hydrogen Energy* **2012**, *37*, 17068–17077. [CrossRef]
150. Li, P.; Liu, C.; Wu, G.; Heng, Y.; Lin, S.; Ren, A.; Lv, K.; Xiao, L.; Shi, W. Solvothermal synthesis and visible light-driven photocatalytic degradation for tetracycline of Fe-doped $SrTiO_3$. *RSC Adv.* **2014**, *4*, 47615–47624. [CrossRef]
151. Wang, J.; Yin, S.; Zhang, Q.; Saito, F.; Sato, T. Influences of the factors on photocatalysis of fluorine-doped $SrTiO_3$ made by mechanochemical method. *Solid State Ion.* **2004**, *172*, 191–195. [CrossRef]
152. Zou, F.; Jiang, Z.; Qin, X.; Zhao, Y.; Jiang, L.; Zhi, J.; Xiao, T.; Edwards, P.P. Template-free synthesis of mesoporous N-doped $SrTiO_3$ perovskite with high visible-light-driven photocatalytic activity. *Chem. Commun.* **2012**, *48*, 8514–8516. [CrossRef] [PubMed]
153. Ruzimuradov, O.; Sharipov, K.; Yarbekov, A.; Saidov, K.; Hojamberdiev, M.; Prasad, R.M.; Cherkashinin, G.; Riedel, R. A facile preparation of dual-phase nitrogen-doped TiO_2–$SrTiO_3$ macroporous monolithic photocatalyst for organic dye photodegradation under visible light. *J. Eur. Ceram. Soc.* **2015**, *35*, 1815–1821. [CrossRef]
154. Xu, J.; Wei, Y.; Huang, Y.; Wang, J.; Zheng, X.; Sun, Z.; Fan, L.; Wu, J. Solvothermal synthesis nitrogen doped $SrTiO_3$ with high visible light photocatalytic activity. *Ceram. Int.* **2014**, *40*, 10583–10591. [CrossRef]
155. Cargnello, M.; Delgado Jaén, J.J.; Hernández Garrido, J.C.; Bakhmutsky, K.; Montini, T.; Calvino Gámez, J.J.; Gorte, R.J.; Fornasiero, P. Exceptional activity for methane combustion over modular Pd@CeO_2 subunits on functionalized Al_2O_3. *Science* **2012**, *337*, 713–717. [CrossRef] [PubMed]
156. Reina, T.R.; Ivanova, S.; Idakiev, V.; Tabakova, T.; Centeno, M.A.; Deng, Q.F.; Yuan, Z.Y.; Odriozola, J.A. Nanogold mesoporous iron promoted ceria catalysts for total and preferential CO oxidation reactions. *J. Mol. Catal. A Chem.* **2016**, *414*, 62–71. [CrossRef]
157. Conner, W.C.; Falconer, J.L. Spillover in Heterogeneous Catalysis. *Chem. Rev.* **1995**, *95*, 759–788. [CrossRef]
158. Bozo, C.; Guilhaume, N.; Herrmann, J.M. Role of the ceria-zirconia support in the reactivity of platinum and palladium catalysts for methane total oxidation under lean conditions. *J. Catal.* **2001**, *203*, 393–406. [CrossRef]
159. An, K.; Alayoglu, S.; Musselwhite, N.; Plamthottam, S.; Lindeman, A.E.; Somorjai, G.A.; Melaet, G. Enhanced CO oxidation rates at the interface of mesoporous oxides and Pt nanoparticles. *J. Am. Chem. Soc.* **2013**, *135*, 16689–16696. [CrossRef] [PubMed]
160. Gatla, S.; Aubert, D.; Agostini, G.; Mathon, O.; Pascarelli, S.; Lunkenbein, T.; Willinger, M.G.; Kaper, H. Room-Temperature CO Oxidation Catalyst: Low-Temperature Metal-Support Interaction between Platinum Nanoparticles and Nanosized Ceria. *ACS Catal.* **2016**, *6*, 6151–6155. [CrossRef]
161. Avila, M.S.; Vignatti, C.I.; Apesteguía, C.R.; Garetto, T.F. Effect of support on the deep oxidation of propane and propylene on Pt-based catalysts. *Chem. Eng. J.* **2014**, *241*, 52–59. [CrossRef]
162. Groppi, G.; Cristiani, C.; Lietti, L.; Ramella, C.; Valentini, M.; Forzatti, P. Effect of ceria on palladium supported catalysts for high temperature combustion of CH_4 under lean conditions. *Catal. Today* **1999**, *50*, 399–412. [CrossRef]
163. Nartova, A.V.; Kovtunova, L.M.; Khudorozhkov, A.K.; Shefer, K.I.; Shterk, G.V.; Kvon, R.I.; Bukhtiyarov, V.I. Influence of preparation conditions on catalytic activity and stability of platinum on alumina catalysts in methane oxidation. *Appl. Catal. A Gen.* **2018**, *566*, 174–180. [CrossRef]
164. Schwartz, W.R.; Pfe, L.D. Combustion of Methane over Palladium-Based Catalysts: Support Interactions. *J. Phys. Chem. C* **2012**, *116*, 8571–8578. [CrossRef]
165. Cargnello, M.; Doan-nguyen, V.V.T.; Gordon, T.R.; Diaz, R.E.; Stach, E.A.; Gorte, R.J.; Fornasiero, P.; Murray, C.B. Control of Metal Nanocrystal Size Reveals Metal-Support Interface Role for Ceria Catalysts. *Science* **2013**, *341*, 771–774. [CrossRef] [PubMed]
166. Pakharukova, V.P.; Pakharukov, I.Y.; Bukhtiyarov, V.I.; Parmon, V.N. Alumina-supported platinum catalysts: Local atomic structure and catalytic activity for complete methane oxidation. *Appl. Catal. A Gen.* **2014**, *486*, 12–18. [CrossRef]
167. Lee, S.; Seo, J.; Jung, W. Sintering-resistant Pt@CeO_2 nanoparticles for high-temperature oxidation catalysis. *Nanoscale* **2016**, *8*, 10219–10228. [CrossRef] [PubMed]
168. Prieto, G.; Zecevic, J.; Friedrich, H.; de Jong, K.P.; de Jong, P.E. Towards stable catalysts by controlling collective properties of supported metal nanoparticles. *Nat. Mater.* **2013**, *12*, 34–39. [CrossRef] [PubMed]
169. Farmer, J.A.; Campbell, C.T. Ceria Maintains Smaller Metal Catalyst Particles by Strong Metal-Support Bonding. *Chem. Mater.* **2010**, *329*, 933–937. [CrossRef]

170. Park, J.E.; Kim, K.B.; Seo, K.W.; Song, K.S.; Park, E.D. Propane combustion over supported Pt catalysts. *Res. Chem. Intermed.* **2011**, *37*, 1135–1143. [CrossRef]
171. Ramirez, A.A.; Benard, S.; Anne, G.-F.; Jones, J.P.; Heitz, M. Treatment of air polluted with methanol vapours in biofilters with and without percolation. *Can. J. Civ. Eng.* **2009**, *36*, 1911–1918. [CrossRef]
172. Liu, Y.; Dai, H.; Du, Y.; Deng, J.; Zhang, L.; Zhao, Z.; Tong, C. Controlled preparation and high catalytic performance of three-dimensionally ordered macroporous $LaMnO_3$ with nanovoid skeletons for the combustion of toluene. *J. Catal.* **2012**, *287*, 149–160. [CrossRef]
173. Zhu, J.; Li, H.; Zhong, L.; Xiao, P.; Xu, X.; Yang, X.; Zhao, Z.; Li, J. Perovskite oxides: Preparation, characterizations, and applications in heterogeneous catalysis. *ACS Catal.* **2014**, *4*, 2917–2940. [CrossRef]
174. Fujishima, A.; Honda, K. Electrochemical photolysis of water at a semiconductor electrode. *Nature* **1972**, *238*, 37–38. [CrossRef] [PubMed]
175. Schneider, J.; Matsuoka, M.; Takeuchi, M.; Zhang, J.; Horiuchi, Y.; Anpo, M.; Bahnemann, D.W. Understanding TiO_2 photocatalysis: Mechanisms and materials. *Chem. Rev.* **2014**, *114*, 9919–9986. [CrossRef] [PubMed]
176. Ohtani, B. Photocatalysis A to Z—What we know and what we do not know in a scientific sense. *J. Photochem. Photobiol. C* **2010**, *11*, 157–178. [CrossRef]
177. Xiao, Z.; Yang, W.; Zhu, J.; Sun, P.; Chen, J.; Li, Y. Porous cube-like $SrTiO_3$ particles self-assembled by primary nanocubes with enhanced photodegradation performance. *J. Electron. Mater.* **2025**, *54*, 3602–3608. [CrossRef]
178. Zheng, Z.; Huang, B.; Qin, X.; Zhang, X.; Dai, Y. Facile synthesis of $SrTiO_3$ hollow microspheres built as assembly of nanocubes and their associated photocatalytic activity. *J. Colloid Interface Sci.* **2011**, *358*, 68–72. [CrossRef] [PubMed]
179. Dong, W.; Li, X.; Yu, J.; Guo, W.; Li, B.; Tan, L.; Li, C.; Shi, J.; Wang, G. Porous $SrTiO_3$ spheres with enhanced photocatalytic performance. *Mater. Lett.* **2012**, *67*, 131–134. [CrossRef]
180. Lai, X.-Y.; Wang, C.-R.; Jin, Q.; Yu, R.-B.; Wang, D. Synthesis and photocatalytic activity of hierarchical flower-like $SrTiO_3$ nanostructure. *Sci. China Mater.* **2015**, *58*, 192–197. [CrossRef]
181. Wang, B.; Shen, S.; Guo, L. $SrTiO_3$ single crystals enclosed with high-indexed {023} facets and {001} facets for photocatalytic hydrogen and oxygen evolution. *Appl. Catal. B Environ.* **2015**, *166–167*, 320–326.
182. Zhou, X.; Liu, N.; Yokosawa, T.; Osvet, A.; Miehlich, M.E.; Meyer, K.; Spiecker, E.; Schmuki, P. Intrinsically activated $SrTiO_3$: Photocatalytic H_2 evolution from neutral aqueous methanol solution in the absence of any noble metal cocatalyst. *ACS Appl. Mater. Interfaces* **2018**, *10*, 29532–29542. [CrossRef] [PubMed]
183. Niishiro, R.; Kato, H.; Kudo, A. Nickel and chromium codoped $SrTiO_3$ photocatalysts for visible-light-induced hydrogen evolution. *Phys. Chem. Chem. Phys.* **2005**, *7*, 2241–2245. [CrossRef] [PubMed]
184. Sankaranarayanan, S.; Dasari, D.S.H.; Kandasamy, P.; Subramanian, S.; Sundaramoorthy, A.; Neti, S. Development of $Ag/SrTiO_3$ and $Ag/SrTiO_3$/GO nanocomposites with superior photocatalytic and electrochemical characteristics for the environmental remediation of industrial dye. *Ceram. Int.* **2024**, *50*, 4218–4226. [CrossRef]
185. Li, X.; Yu, J.; Jaroniec, M.; Chen, X. Cocatalysts for selective photoreduction of CO_2 into solar fuels. *Chem. Rev.* **2019**, *119*, 3962–4179. [CrossRef] [PubMed]
186. Xu, Y.; Schoonen, M.A.A. The absolute energy positions of conduction and valence bands of selected semiconducting minerals. *Am. Mineral.* **2000**, *85*, 543–556. [CrossRef]
187. Jia, Y.; Zhao, D.; Li, M.; Han, H.; Li, C. La and Cr co-doped $SrTiO_3$ as an H_2 evolution photocatalyst for construction of a Z-scheme overall water splitting system. *Chin. J. Catal.* **2018**, *39*, 421–430. [CrossRef]
188. Nunes, M.J.; Lopes, A.; Pacheco, M.J.; Ciríaco, L. Visible-light-driven AO7 photocatalytic degradation and toxicity removal at Bi-doped $SrTiO_3$. *Materials* **2022**, *15*, 2465. [CrossRef] [PubMed]
189. Yang, D.; Zou, X.; Sun, Y.; Tong, Z.; Jiang, Z. Fabrication of three-dimensional porous La-doped $SrTiO_3$ microspheres with enhanced visible light catalytic activity for Cr(VI) reduction. *Front. Chem. Sci. Eng.* **2018**, *12*, 440–449. [CrossRef]
190. Xing, G.; Zhao, L.; Sun, T.; Su, Y.; Wang, X. Hydrothermal derived nitrogen doped $SrTiO_3$ for efficient visible light driven photocatalytic reduction of chromium(VI). *SpringerPlus* **2016**, *5*, 1132. [CrossRef] [PubMed]
191. Pan, L.; Mei, H.; Zhu, G.; Li, S.; Xie, X.; Gong, S.; Liu, H.; Jin, Z.; Gao, J.; Cheng, L.; et al. Bi selectively doped $SrTiO_{3-x}$ nanosheets enhance photocatalytic CO_2 reduction under visible light. *J. Colloid Interface Sci.* **2022**, *611*, 137–148. [CrossRef] [PubMed]
192. Aravinthkumar, K.; John Peter, I.; Anandha Babu, G.; Navaneethan, M.; Karazhanov, S.; Raja Mohan, C. Enhancing the short circuit current of a dye-sensitized solar cell and photocatalytic dye degradation using Cr doped $SrTiO_3$ interconnected spheres. *Mater. Lett.* **2022**, *319*, 132284. [CrossRef]
193. Low, J.; Yu, J.; Jaroniec, M.; Wageh, S.; Al-Ghamdi, A.A. Heterojunction photocatalysts. *Adv. Mater.* **2017**, *29*, 1601694. [CrossRef]
194. Wang, Q.; Domen, K. Particulate photocatalysts for light-driven water splitting: Mechanisms and recent advances. *Chem. Rev.* **2020**, *120*, 919–985. [PubMed]
195. Chen, X.; Shen, S.; Guo, L.; Mao, S.S. Semiconductor-based photocatalytic hydrogen generation. *Chem. Rev.* **2010**, *110*, 6503–6570. [CrossRef] [PubMed]

196. Ran, J.; Zhang, J.; Yu, J.; Jaroniec, M.; Qiao, S.Z. Earth-abundant cocatalysts for semiconductor-based photocatalytic water splitting. *Chem. Soc. Rev.* **2014**, *43*, 7787–7812. [PubMed]
197. Zhang, N.; Zhang, Y.; Xu, Y.J. Recent progress on graphene-based photocatalysts. *Nanoscale* **2012**, *4*, 5792–5813. [CrossRef] [PubMed]
198. Xiang, Q.; Yu, J.; Jaroniec, M. Graphene-based semiconductor photocatalysts. *Chem. Soc. Rev.* **2012**, *41*, 782–796. [CrossRef] [PubMed]
199. Zhao, L.; Lam, S.-M.; Ong, Y.T.; Sin, J.-C.; Zeng, H.; Xie, Q.; Lim, J.W. $FeWO_4$ coupling on cube-like $SrTiO_3$ as a highly active S-scheme heterojunction composite for visible light photocatalysis and antibacterial applications. *Environ. Technol. Innov.* **2022**, *28*, 102941.
200. Xia, Y.; He, Z.; Lu, Y.; Tang, B.; Sun, S.; Su, J.; Li, X. Fabrication and photocatalytic property of magnetic $SrTiO_3/NiFe_2O_4$ heterojunction nanocomposites. *RSC Adv.* **2018**, *8*, 5441–5450. [CrossRef] [PubMed]
201. Cheng, C.; Wang, J.; Zhao, Z.; Chen, C.; Cui, S.; Wang, Y.; Pan, L.; Ni, Y.; Lu, C. S-scheme $SrTiO_3$/porous ZnO derived by pyrolysis of ZIF-8 composite with efficient photocatalytic activity for pollutant degradation. *J. Alloys Compd.* **2022**, *896*, 163064. [CrossRef]
202. Hu, C.; Huang, H.-X.; Lin, Y.-F.; Yoshida, M.; Chen, T.-H. Decoration of $SrTiO_3$ nanofibers by BiOI for photocatalytic methyl orange degradation under visible light irradiation. *J. Taiwan Inst. Chem. Eng.* **2019**, *96*, 264–272. [CrossRef]
203. Xu, X.; Chen, C.; Shu, L.; Cheng, C.; Tang, Z.; Wang, Y.; Pan, L.; Guan, Z. Anchoring $SrTiO_3$ nanoparticles on layered $ZnIn_2S_4$ to construct S-scheme heterojunctions as novel photocatalysts for efficient degradation of MO dye. *FlatChem* **2023**, *41*, 100526. [CrossRef]
204. Wang, X.; Jiang, L.; Li, K.; Wang, J.; Fang, D.; Zhang, Y.; Tian, D.; Zhang, Z.; Dionysiou, D.D. Fabrication of novel Z-scheme $SrTiO_3/MnFe_2O_4$ system with double-response activity for simultaneous microwave-induced and photocatalytic degradation of tetracycline and mechanism insight. *Chem. Eng. J.* **2020**, *400*, 125981. [CrossRef]
205. Alshammari, M.S.; Hassan, W.H.; Al-Zahiwat, M.M.; Osman, H.; El-Sabban, H.A.; Diab, M.A.; Atamuratova, Z.; Saitov, E.; Amari, A. Novel environmentally benign dual Z-scheme $SrTiO_3/g\text{-}C_3N_4/ZnO$ heterojunction for efficient H_2 evolution and polluted water treatment: Optimization, mechanism interpretations and toxicity assessment. *FlatChem* **2025**, *50*, 100841. [CrossRef]
206. Konstas, P.-S.; Konstantinou, I.; Petrakis, D.; Albanis, T. Synthesis, characterization of $g\text{-}C_3N_4/SrTiO_3$ heterojunctions and photocatalytic activity for organic pollutants degradation. *Catalysts* **2018**, *8*, 554. [CrossRef]
207. Wu, X.; Chen, J.; Yang, X.; Zheng, H.; Ma, Y.; Li, Y. Synergistic activation of peroxymonosulfate for tetracycline hydrochloride degradation with $SrTiO_3/Ti_3C_2T_x$ photocatalyst. *Appl. Surf. Sci.* **2025**, *680*, 161317. [CrossRef]
208. Gopal, V.; Palanisamy, G.; Lee, J.; Abu-Yousef, I.A.; Majdalawieh, A.F.; Mahasneh, A.; Prabu, K.M.; Kanan, S. Fabrication of $SrTiO_3$ anchored $rGO/g\text{-}C_3N_4$ photocatalyst for the removal of mixed dye from wastewater: Dual photocatalytic mechanism. *Sci. Rep.* **2024**, *14*, 16259. [CrossRef] [PubMed]
209. Atkinson, I.; Parvulescu, V.; Pandele Cusu, J.; Anghel, E.M.; Voicescu, M.; Culita, D.; Somacescu, S.; Munteanu, C.; Šćepanović, M.; Popovic, Z.V.; et al. Influence of preparation method and nitrogen (N) doping on properties and photocatalytic activity of mesoporous $SrTiO_3$. *J. Photochem. Photobiol. A Chem.* **2019**, *368*, 41–51. [CrossRef]
210. Li, J.; Wang, F.; Meng, L.; Han, M.; Guo, Y.; Sun, C. Controlled synthesis of $BiVO_4/SrTiO_3$ composite with enhanced sunlight-driven photofunctions for sulfamethoxazole removal. *J. Colloid Interface Sci.* **2017**, *485*, 116–122. [CrossRef] [PubMed]
211. Ji, W.; Shen, T.; Kong, J.; Rui, Z.; Tong, Y. Synergistic performance between visible-light photocatalysis and thermocatalysis for VOCs oxidation over robust Ag/F-codoped $SrTiO_3$. *Ind. Eng. Chem. Res.* **2018**, *57*, 12766–12773. [CrossRef]
212. Grabowska, E.; Marchelek, M.; Klimczuk, T.; Lisowski, W.; Zaleska-Medynska, A. $TiO_2/SrTiO_3$ and $SrTiO_3$ microspheres decorated with Rh, Ru or Pt nanoparticles: Highly UV–vis responsive photoactivity and mechanism. *J. Catal.* **2017**, *350*, 159–173. [CrossRef]
213. Kumar, A.; Rana, A.; Sharma, G.; Naushad, M.; Al-Muhtaseb, A.H.; Guo, C.; Iglesias-Juez, A.; Stadler, F.J. High-performance photocatalytic hydrogen production and degradation of levofloxacin by wide spectrum-responsive Ag/Fe_3O_4-bridged $SrTiO_3/g\text{-}C_3N_4$ plasmonic nanojunctions: Joint effect of Ag and Fe_3O_4. *ACS Appl. Mater. Interfaces* **2018**, *10*, 40474–40490. [CrossRef] [PubMed]
214. Faisal, M.; Harraz, F.A.; Ismail, A.A.; El-Toni, A.M.; Al-Sayari, S.A.; Al-Hajry, A.; Al-Assiri, M.S. Polythiophene/mesoporous $SrTiO_3$ nanocomposites with enhanced photocatalytic activity under visible light. *Sep. Purif. Technol.* **2018**, *190*, 33–44. [CrossRef]
215. Yang, D.; Sun, Y.; Tong, Z.; Nan, Y.; Jiang, Z. Fabrication of bimodal-pore $SrTiO_3$ microspheres with excellent photocatalytic performance for Cr(VI) reduction under simulated sunlight. *J. Hazard. Mater.* **2016**, *312*, 45–54. [CrossRef] [PubMed]
216. Neti, S.; Nanmangalam, A.R.; Chintakuntla, C.N.; Ramasamy, T.; Sankaranarayanan, S. Structural influence of strontium titanate nanocubes for photocatalytic dye degradation and electrochemical applications. *Inorg. Chem. Commun.* **2023**, *148*, 110299. [CrossRef]
217. Goto, Y.; Hisatomi, T.; Wang, Q.; Higashi, T.; Ishikiriyama, K.; Maeda, T.; Akiyama, S. A particulate photocatalyst water-splitting panel for large-scale solar hydrogen generation. *Joule* **2018**, *2*, 509–520. [CrossRef]

218. Asai, R.; Nemoto, H.; Jia, Q.; Saito, K.; Iwase, A.; Kudo, A. A visible-light responsive rhodium and antimony-codoped $SrTiO_3$ powdered photocatalyst loaded with an IrO_2 cocatalyst for solar water splitting. *Chem. Commun.* **2014**, *50*, 2543–2546. [CrossRef]
219. Lyu, H.; Hisatomi, T.; Goto, Y.; Yoshida, M.; Higashi, T.; Katayama, M.; Sakata, Y. An Al-doped $SrTiO_3$ photocatalyst maintaining sunlight-driven overall water splitting activity for over 1000 h of constant illumination. *Chem. Sci.* **2019**, *10*, 3196–3201. [CrossRef] [PubMed]
220. Niishiro, R.; Kudo, A. Development of visible-light-driven TiO_2 and $SrTiO_3$ photocatalysts doped with metal cations for H_2 or O_2 evolution. *Solid State Phenom.* **2010**, *162*, 29–40. [CrossRef]
221. Guan, X.; Guo, L. Cocatalytic effect of $SrTiO_3$ on Ag_3PO_4 toward enhanced photocatalytic water oxidation. *ACS Catal.* **2014**, *4*, 3020–3026. [CrossRef]
222. Patial, S.; Hasija, V.; Raizada, P.; Singh, P.; Khan Singh, A.A.P.; Asiri, A.M. Tunable photocatalytic activity of $SrTiO_3$ for water splitting: Strategies and future scenario. *J. Environ. Chem. Eng.* **2020**, *8*, 103791. [CrossRef]
223. Fareed, I.; Farooq, M.U.H.; Khan, M.D.; Ali, Z.; Butt, F.K. Band gap engineering of Strontium Titanate ($SrTiO_3$) for improved photocatalytic activity and excellent bio-sensing aptitude. *Mater. Sci. Semicond. Process.* **2024**, *177*, 108327. [CrossRef]
224. Wang, X.; Xu, Q.; Li, M.; Shen, S.; Wang, X.; Wang, Y.; Feng, Z.; Shi, J.; Han, H.; Li, C. Photocatalytic overall water splitting promoted by an α–β phase junction on Ga_2O_3. *Angew. Chem. Int. Ed.* **2012**, *51*, 13089–13092. [CrossRef] [PubMed]
225. Kőrösi, L.; Bognár, B.; Czégény, G.; Lauciello, S. Phase-selective synthesis of anatase and rutile TiO_2 nanocrystals and their impacts on grapevine leaves: Accumulation of mineral nutrients and triggering the plant defense. *Nanomaterials* **2022**, *12*, 483. [CrossRef] [PubMed]
226. Žerjav, G.; Albreht, A.; Vovk, I.; Pintar, A. Revisiting terephthalic acid and coumarin as probes for photoluminescent determination of hydroxyl radical formation rate in heterogeneous photocatalysis. *Appl. Catal. A Gen.* **2020**, *598*, 117566. [CrossRef]
227. Nosaka, Y.; Nosaka, A.Y. Generation and detection of reactive oxygen species in photocatalysis. *Chem. Rev.* **2017**, *117*, 11302–11336. [CrossRef] [PubMed]
228. Ahmed, S.; Hasan, T.; Faysal, A.K.M.S.H.; Nishat, S.S.; Khan, M.N.I.; Kabir, A.; Ahmed, I. A DFT+U approach to doped $SrTiO_3$ for solar harvesting applications. *Comput. Mater. Sci.* **2022**, *214*, 111743. [CrossRef]
229. Holmström, E.; Spijker, P.; Foster, A.S. The interface of $SrTiO_3$ and H_2O from density functional theory molecular dynamics. *Proc. Math. Phys. Eng. Sci.* **2016**, *472*, 20160293. [CrossRef] [PubMed]
230. Jiang, Y.; Zhang, J.; Zhang, X.; Ma, Y. Mechanistic insights into the role of empty mid-gap states in Al- and Rh-doped $SrTiO_3$ for photocatalytic water splitting. *Appl. Surf. Sci.* **2025**, *694*, 162832. [CrossRef]
231. Shabbir, A.; Sardar, S.; Mumtaz, A. Mechanistic investigations of emerging type-II, Z-scheme and S-scheme heterojunctions for photocatalytic applications—A review. *J. Alloys Compd.* **2024**, *1003*, 175683. [CrossRef]
232. Zhao, X.; Xiao, S.; Yao, B.; Chen, Y.; Yu, S. DFT-based mechanistic exploration and application in photocatalytic heterojunctions. *J. Chem. Theory Comput.* **2024**, *20*, 9770–9786. [CrossRef] [PubMed]

Disclaimer/Publisher's Note: The statements, opinions and data contained in all publications are solely those of the individual author(s) and contributor(s) and not of MDPI and/or the editor(s). MDPI and/or the editor(s) disclaim responsibility for any injury to people or property resulting from any ideas, methods, instructions or products referred to in the content.